Improvement of thrust performance in ion engine with argon propellant by numerical analysis

胡, 澤豊
九州大学大学院総合理工学府先端エネルギー理工学専攻

２０２１

Master's Thesis

Department of Advanced Energy Engineering Science,

Interdisciplinary Graduate School of Engineering Sciences,

Kyushu University

Title

Improvement of thrust performance in ion engine with argon propellant by numerical analysis

Name HU ZEFENG

Supervisor YAMAMOTO NAOJI

CONTENT

1.Introduction

1.1 Background

In the past fifty years, space exploration has been regarded as a major project of the whole country. However, with the entry of many emerging powers into the space business in the 21st century, the market is now experiencing unprecedented expansion.[1-1)~1-4)] Micro/small satellites are one of the reasons why emerging countries, private companies, as well as universities and numerous research institutions have been able to enter the space development market, and have grown significantly from it. Micro-satellites generally weigh less than 50kg, and have the advantages of being able to be developed at low cost (tens of millions of dollars) and having a short development cycle (about two or three years). Micro-satellites also have the advantage of being small, lightweight, and relatively low risk of failure compared to large satellites weighing several tons in the past.[1-5)~1-6)] Therefore, while being vigorously developed by various parties, micro-satellites have also become natural experimental devices for new technologies.

Electric propulsion is a general term for a series of propulsion forms that obtains a reaction force by applying electrical energy to the propellant. Unlike rocket thruster that use conventional chemical reaction conversion capabilities, it can use electrostatic force and electromagnetic force to achieve thrust conversion, thus achieving an order of magnitude or more specific impulse (thrust produced by a unit weight flow of propellant): The first-stage main rocket engine Vulcan 2 of the EU heavy launch vehicle Ariane 5 has a nozzle velocity of 4230m/s and a specific impulse of 431 seconds. And NASA's Evolutionary Xenon Thruster (NEXT) ion jet engine with xenon as propellant has a nozzle speed of 40km/s and a specific impulse of 4300 seconds, ten times that of Vulcan 2.[1-7)~1-8)]

As one of the typical electric propulsion devices currently in use, the ion engine is suitable for the attitude control of current micro-satellites and the main propulsion method of small detectors due to its long application time(The first mercury-propellant ion engine was built at NASA in 1959 and successfully tested.), well-developed and higher specific impulse.

However, the ion engine's fuss about propellant has become one of the reasons that hinder its development. So far, mercury, cesium, xenon, argon and other elements have become options for propellants, among which mercury and cesium have been eliminated due to their corrosiveness and toxicity. As the most widely used ion engine propellant at

present, xenon gas has excellent performance, but it also has disadvantages such as low reserves and high cost of use. (The reserves of xenon gas in the atmosphere are only 8.6 parts per billion. The price of xenon gas on the international market has grown from about $6,000 per cubic meter in 2005 to $20,000 per cubic meter today.) Therefore, the search for an ion engine propellant to replace xenon is indispensable for its development. Argon occupies 0.934% of the Earth's atmosphere by volume, and today's international market price is only $0.4 per cubic meter.Considering that the small detector Deep Space One, which was launched by NASA in 1998, needs to consume 100g of xenon per day. In order to achieve a larger specific impulse, the small thruster put into use in the future will inevitably consume more xenon, and the consumption of propellant alone will be relatively large. Argon gas has the advantages of huge reserves and low price at the same time. Also, due to its inert chemical nature, it does not cause damage to the thruster components. Therefore, it can be regarded as a good alternative to xenon as an ion engine propellant.

1.2. Ion engine principle

Figure 1-1 shows a conceptual diagram of the ion engine. The ion engine heats and ionizes the propellant by arc discharge or microwave to generate plasma, and applies a high voltage of about 1000V to the porous electrode composed of 2 or 3 electrodes to accelerate the ions. It is an electrostatic acceleration type propulsion device. The ion engine consists of three main areas.

① Ionizer for ionized propellant

② An accelerator unit that electrostatically accelerates the generated ions to obtain thrust

③ Neutralizer that neutralizes the emitted ion beam

Each of these processes is performed by an ion source, an accelerating electrode, and a neutralizer, respectively.

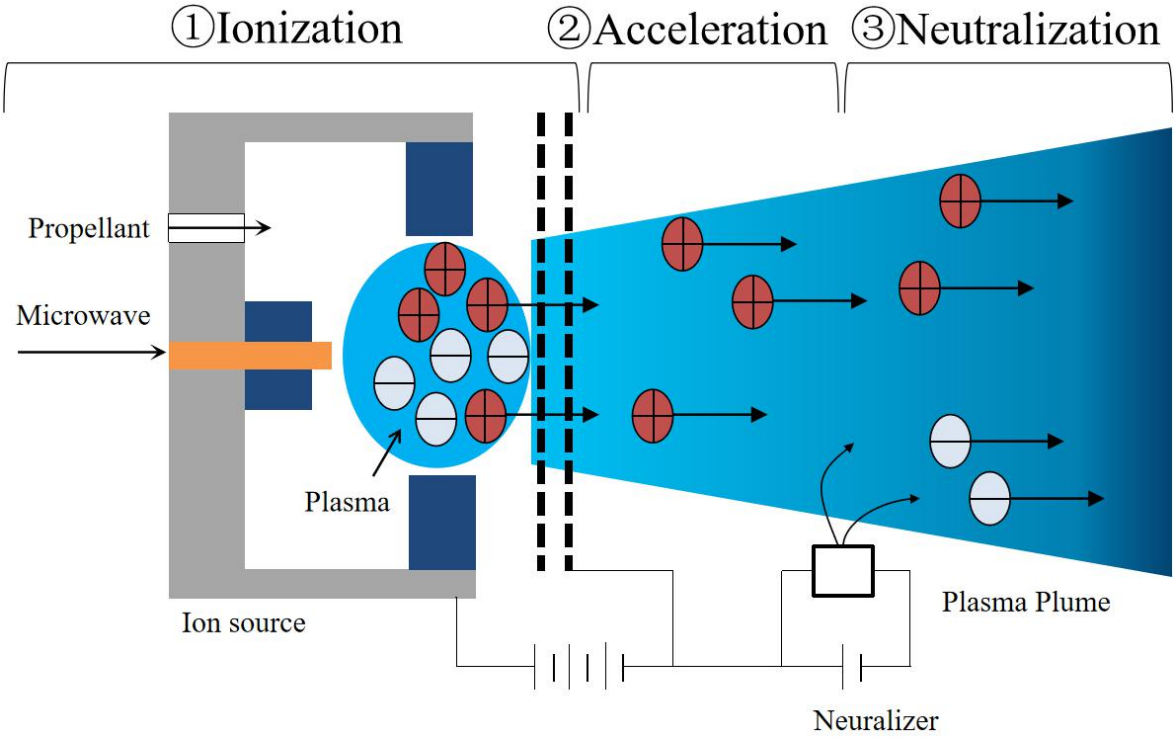

Fig. 1-1 Conceptual diagram of ion engine

1.2.1 Microwave discharge ion engine

The ion engine is classified into a DC discharge type and a microwave discharge type according to the plasma generation method. Microwave discharge means that electrons are accelerated by an AC electric field in the microwave band. Due to neutral particles and impact ionization, the number of electrons increases, and the gas becomes plasma and remains discharged. Compared with DC discharge, this microwave discharge has the following advantages.

(1) Electrodes are not required for plasma generation, and there is no limit to engine life.

(2) Since no heater is used, preheating is not required and the engine can be started immediately.

(3) Since one microwave power source can generate plasma in multiple engines, the system configuration is simplified, the reliability is improved, and the weight of the satellite is reduced.

1.2.2 Plasma generation

Figure 1-3 and figure 1-4 shows the cross-sectional view of the cubic microwave discharge chamber. The microwave discharge in this thruster is characterized by the central conductor of the coaxial cable being inserted directly into the plasma. The outer conductor

of the coaxial cable is connected to the wall of the discharge chamber. In this way, high-density plasma with cut-off density or higher can be generated with low power consumption. The central conductor part is called the antenna, and a strong electric field is generated in the vicinity of the antenna. Magnetic circuits, on the other hand, consist of magnets and soft iron, and electrons are trapped in this magnetic field. In the soft iron part, the part on the plasma discharge side (downstream side) is called the front yoke, and the part on the upstream side is called the back yoke. In the back yoke, the cylindrical part surrounding the antenna is called the central yoke. The region where electrons are trapped between the central yoke and the front yoke is called the magnet tube. Magnetic mirrors are formed at both ends of the region, and electrons are reflected at both ends of the tube under the action of the magnetic mirror and the sheath near the wall, and reciprocate in the region. Therefore, even though it is accelerated by the microwave electric field, it is heated to an energy higher than the ionization energy of the propellant without dissipating.

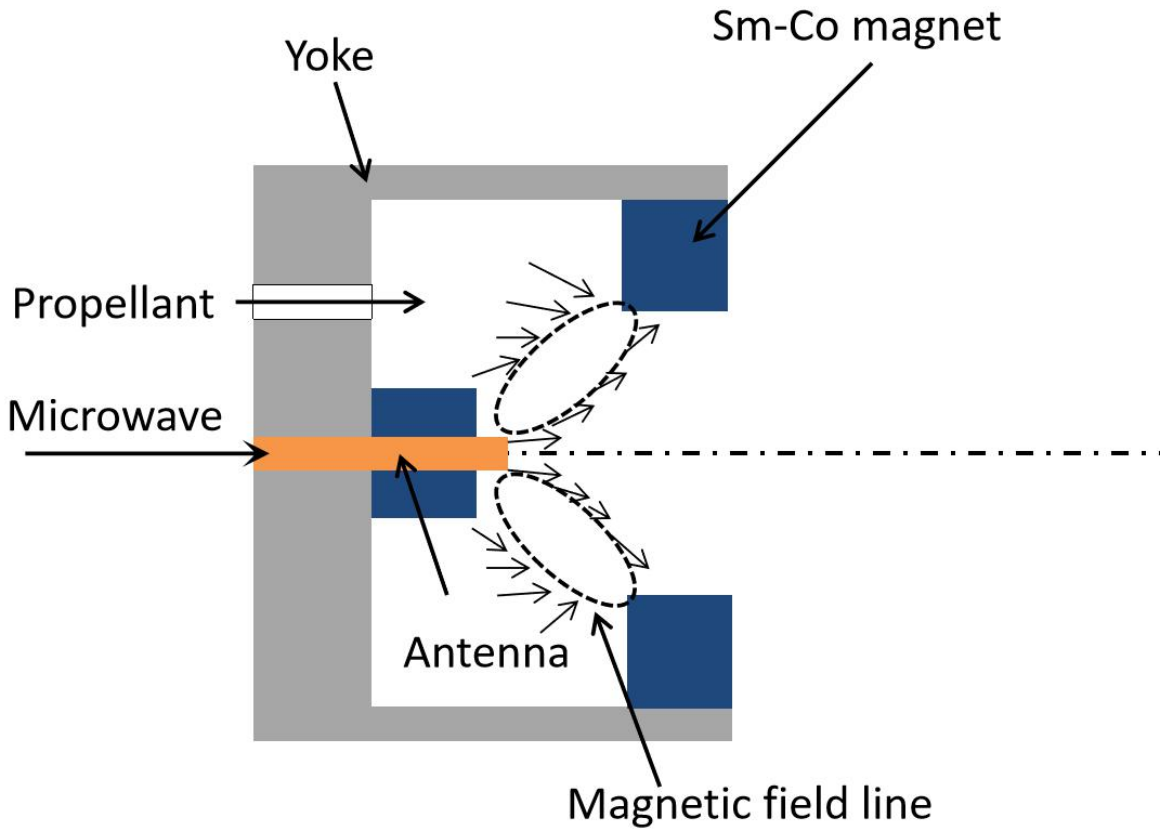

Fig. 1-3 Cross section of a cubic microwave discharge chamber(Y-Z plane)

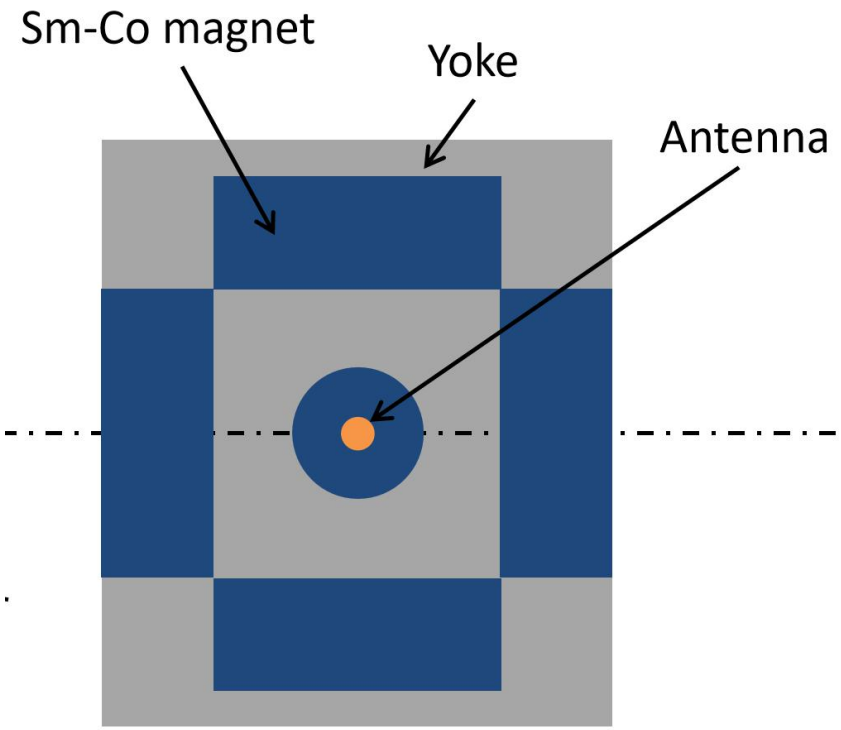

Fig. 1-4 Cross section of a cubic microwave discharge chamber(X-Y plane)

1.3 Previous research

So far, our laboratory has carried out a large number of experiments on the microwave discharge type small ion engine using xenon, argon and krypton as propellants. And many experiments were carried out for different factors such as the magnetic field strength inside the microwave discharge chamber, the shape of the antenna, and the shape of the discharge chamber.[1-9)~1-11)]

In particular, the results of experiments using different propellants in a miniature cylindrical microwave discharge chamber shown in figure 1-5 and figure 1-6 are that argon as a propellant can output a larger ionic current than xenon under appropriate conditions (input power, mass flow, etc.), which means that argon has the possibility to replace xenon.[1-12)]

However, these experiments have yet to elucidate how the physical mechanisms within the discharge chamber change as a result of the shape change, and why it affects performance. The reason is that due to the small size of the engine itself, inserting a device such as an electrostatic probe would cause the plasma in the discharge chamber to interfere, making accurate measurements impossible. Therefore, numerical analysis is a very effective means. Due to the development of computers in recent years, it has become

possible to obtain information that cannot be obtained by experiments. The results allow for research and development while reducing the time and financial cost of experimentation. Using the 3D numerical analysis code developed in this laboratory, the relative interaction between electrons and microwaves is analyzed, thereby revealing the physical mechanism of plasma changes in the discharge chamber.[1-13] Fig. 1-7 and Fig. 1-8 shows the past computational simulation research on the configuration of the discharge chamber in this laboratory, which revealed the direction of improving the discharge chamber of the ion engine by comparing the ion beem current of different discharge chamber lengths and the magnetic field strength in the chamber.[1-14]

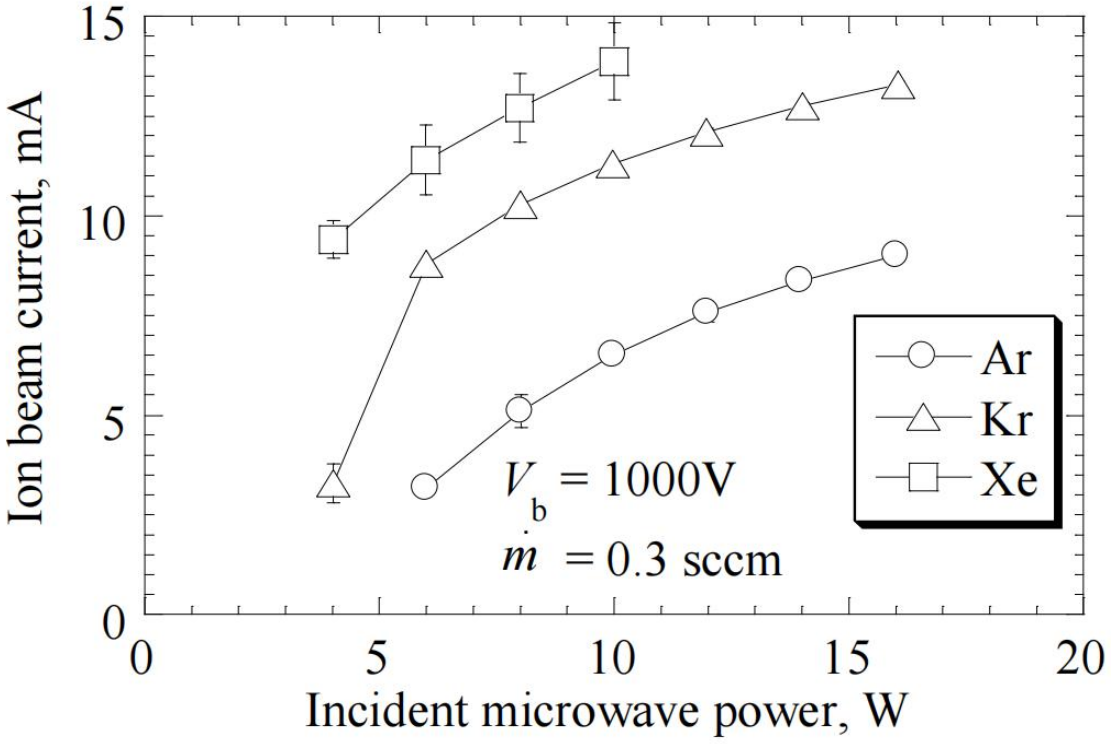

Fig. 1-5 Ion beam current of three gas in a miniature thruster
[N. YAMAMOTO et al.: Development of a Microwave Discharge Ion Thruster Using Argon. Pb_122. Trans. JSASS Space Tech. Japan Vol.7, No. ists 26(2009)]

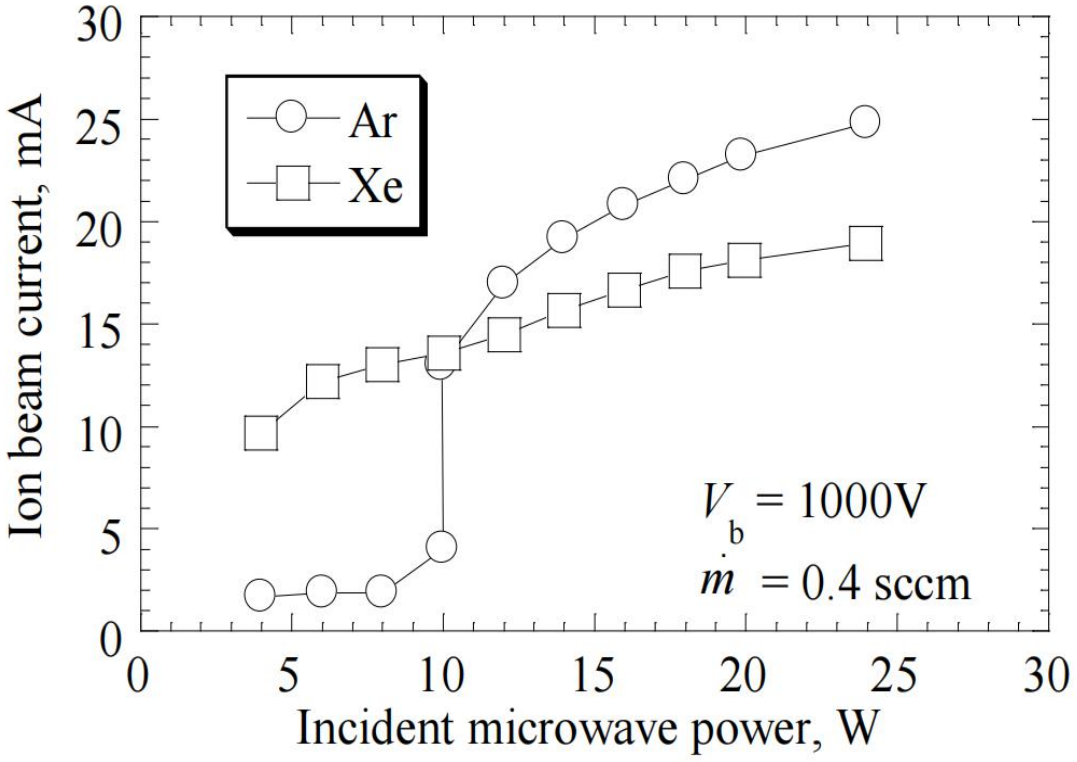

Fig. 1-6 Ion beam current of xenon and argon in a miniature thruster
[N. YAMAMOTO et al.: Development of a Microwave Discharge Ion Thruster Using Argon. Pb_123. Trans. JSASS Space Tech. Japan Vol.7, No. ists 26(2009)]

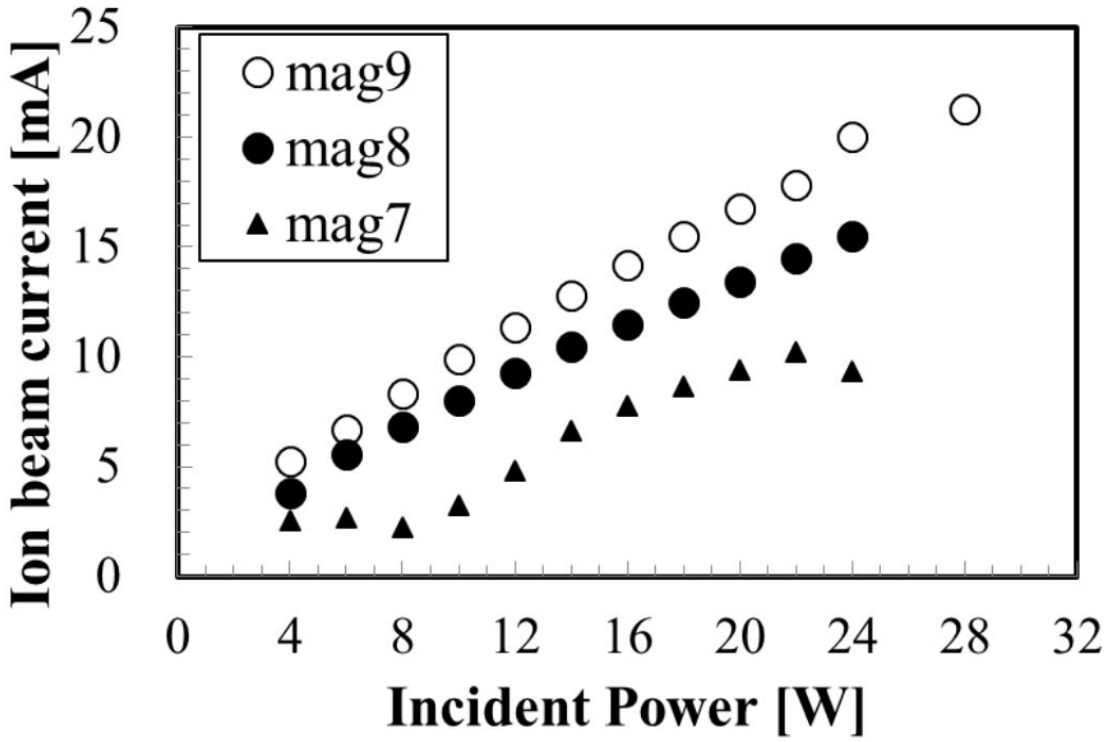

Fig. 1-7 Ion beam current with each magnetic field strength
[Koichi Ushio, "Study on Microwave Discharge Plasma Thruster", P104, 2018 Doctoral Dissertation, Kyushu University.]

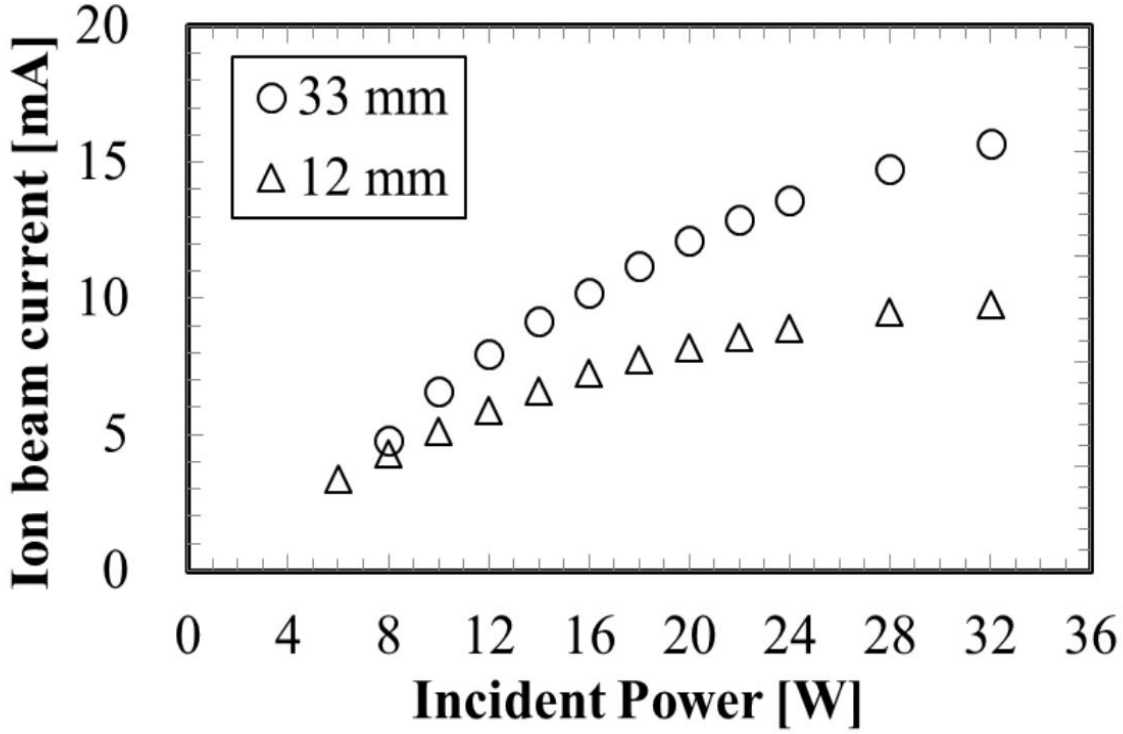

Fig. 1-8 Ion beam current vs. incident power for two discharge chamber lengths for 41 μg/sec.(Error bar is smaller than marker)
[Koichi Ushio, "Study on Microwave Discharge Plasma Thruster", P42, 2018 Doctoral Dissertation, Kyushu University.]

1.4 Research purpose

Based on the above background, the purpose of this study was to simulate the plasma inside the discharge chamber with different propellants (xenon/argon) using a 3D numerical analysis code, and to study the effect of the antenna shape on the interior of the discharge chamber. In order to contrast with the previous experiments, the object simulated in this study is the cubic chamber shown in Fig. 1-3.

This paper consists of the following four chapters.

Chapter 1 describes the latest trends in astronautics, examining the advantages of small thrusters, and the need to find alternatives to xenon as an ion engine propellant. After that, the principle of the ion engine, the research progress so far, and the research method using numerical simulation are also described.

Chapter 2 introduces the specific principles of the numerical simulation method used in the research and the selection and adjustment of each parameter in detail. The FDTD method is the solution of Maxwell's equations used in this study, the collision calculation method used to calculate the motion of charged particles, and the details of the PIC method. In addition, the coupling method and various boundary conditions for these calculations are explained.

Chapter 3 studies the comparison of two propellants, xenon and argon, using the performance of the ion engine as an index in the cubic chamber. At the same time, the effects of different antenna shapes on the performance of the ion engine under different propellant conditions were also studied.

Chapter 4 gives the conclusion and future outlook of this paper.

Reference

1-1) Axelspace Corporation; https://www.axelspace.com/

1-2) Planet Labs, Inc; https://www.planet.com/

1-3) Sastrokusumo, R. Lumanto, “LAPAN A2 Micro Satellite and the Need for Rapid Emergency Communication”, 29th International Symposium on Space Technology and Science, 2013-f-40, 2013.

1-4) UHiroyuki Koizumi, Kimiya Komurasaki, Junichi Aoyama and Koji Yamaguchi, “Engineering Model of the Miniature Ion Propulsion System for the Nano-satellite:

HODOYOSHI-4 ”, Trans. JSASS Aerospace Tech. Japan, Vol. 12, No. ists29, pp. Tb_19-Tb_24, 2014.

1-5) Philip D., David R., Oliver T., Andy B. and Alex da S. C., “Vertical Launch of Small Satellites from the UK”, Proceeding of 67th International Astronautical Congress, IAC-16-B4.5.5, 2016.

1-6) Peter N. Randal, Rhodri A. Lewis and Stephen D. Clark, “QinetiQ T5 based Electric Propulsion System and Architectural Options for Future Applications”, Proceedings of at the 35th International Electric Propulsion Conference, IEPC-2017-170.

1-7) Patterson M, Foster J, Haag T, et al. NEXT: NASA's Evolutionary Xenon Thruster[C]//38th AIAA/ASME/SAE/ASEE Joint Propulsion Conference & Exhibit. 2002: 3832.

1-8) Cuentas-Gallegos A K, López-Cortina S, Brousse T, et al. Electrochemical study of H 3 PMo 12 retention on Vulcan carbon grafted with NH 2 and OH groups[J]. Journal of Solid State Electrochemistry, 2016, 20(1): 67-79.

1-9) N. Yamamoto, H. Kataharada, H. Masui, H. Ijiri and H. Nakashima, AJCPP2005-22093, 2005.

1-10) N. Yamamoto, H. Kataharada, T. Chikaoka, H. Masui and H. Nakashima, IEPC-2005-036, 2005.

1-11) T. Chikaoka, S. Kondo, N. Yamamoto, H. Nakashima and Y. Takao, Proceedings of the 25th International Symposium on Space Technology and Science, 2006, pp.254-259.

1-12) Yamamoto N, Miyoshi M, Takao Y, et al. Development of a Microwave Discharge Ion Thruster Using Argon[J]. TRANSACTIONS OF THE JAPAN SOCIETY FOR AERONAUTICAL AND SPACE SCIENCES, SPACE TECHNOLOGY JAPAN, 2009, 7(ists26): Pb_119-Pb_124.

1-13) Hirokazu Masui, "Numerical analysis of plasma source for microwave discharge type space propulsion", 2005 doctoral dissertation at Kyushu University.

1-14) Koichi Ushio, "Study on Microwave Discharge Plasma Thruster", 2018 Doctoral Dissertation, Kyushu University.

2.Numerical simulation method

In the experiments described in the previous chapter, it was found that the simulation of the plasma behavior of xenon and argon as propellants under different operating conditions is crucial to verify the performance of argon. So this chapter will not only explain the full picture of the code being developed, but also detail the 3D FDTD-PIC-MCC code used for this electronic heating.

2.1 Overall simulation flow

In our laboratory, code development is underway to perform (coupled) computations by combining the two codes shown in Table. 2-1.

Table. 2-1 Simulation model

Research object	Model
Energy acquisition analysis of electrons by interaction between electron and microwave	3D FDTD-PIC-MCC
Calculation of the behavior and electrostatic field of ions and electrons	2D Full-PIC-MCC

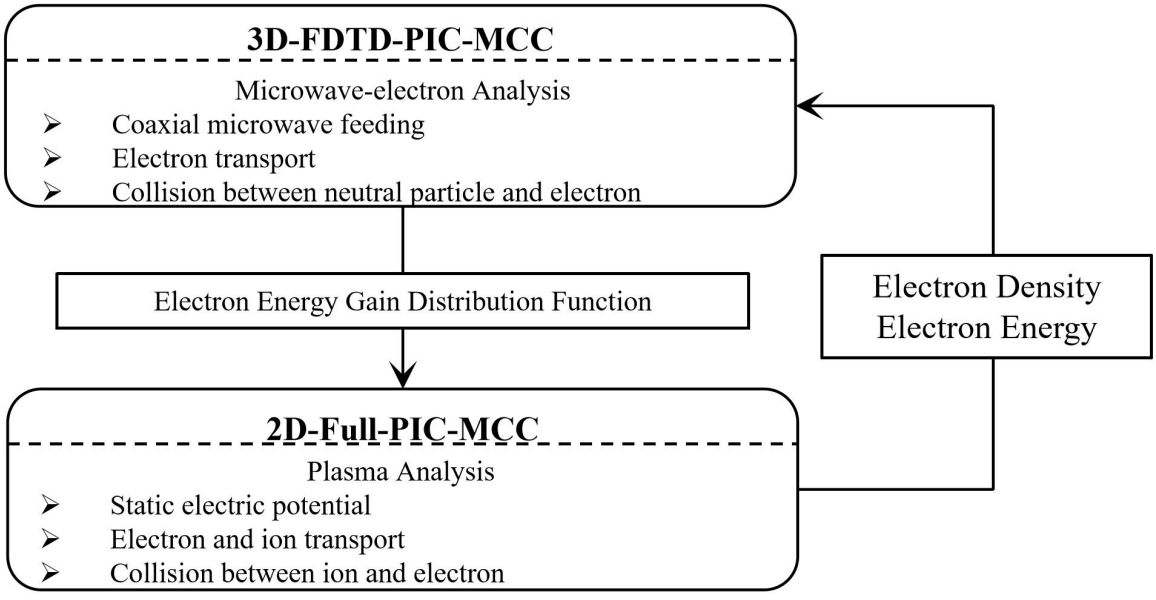

Fig. 2-1 Overflow of the coupling code method

The method of coupling these codes is called weak coupling because it addresses different physical phenomena and exchanges data separately at different time steps. Figure 2-1 shows how these codes are coupled.

To explain in detail, first of all, as mentioned in the previous chapter, the basic principle of the microwave discharge ion engine is the ECR resonance between the permanent magnet and the microwave, so the information of the static magnetic field is required. The static magnetic field distribution when the permanent magnet is placed on the thruster is calculated using commercially available software (described later) before starting the analysis. With this static magnetic field data, subsequent calculations for FDTD-PIC-MCC and Full-PIC-MCC can be performed. In FDTD-PIC-MCC, the absorption of electrons and microwaves is calculated starting from the homogeneous state, and the probability of obtaining electron energy is calculated.

This computes the electron energy increment per unit volume per unit time as a probability density distribution, which is then passed to Full-PIC-MCC as the effect of electron microwave absorption. In Full-PIC-MCC, ions and electrons are calculated starting from a homogeneous state, and particle transport due to electrostatic field effects is analyzed. When the plasma density changes, a distribution above the cut-off density (the density at which the electromagnetic field is practically impenetrable) occurs, and the density distribution changes, thereby changing the amount of microwave absorption by the electrons. In fact, in the calculations of Full-PIC-MCC, if the energy is continuously applied with the initial electron energy acquisition probability, the electron temperature will increase due to the continuous energy transfer from the microwave to the electrons in the specific region.

Therefore, by feeding back the change in plasma density to the FDTD-PIC-MCC again, the effect of cutoff is taken into account, and the variation of microwave propagation caused by the spatial distribution of electron density is considered. In addition, for energy conservation, the electron energy in the Full-PIC-MCC calculation is also fed back. In the calculation of Full-PIC-MCC, the steady state is reached by repeating the calculation, while feeding back to FDTD-PIC-MCC with the sequential change of plasma density. In this way, weakly coupled analysis is the process of independently computing phenomena at different time scales and communicating each result. Since the Full-PIC-MCC code has not been completed at this stage, only 3D-FDTD-PIC-MCC is used for calculation, and the electronic heating characteristics are analyzed using three antenna shapes.

2.2 3D-FDTD-PIC-MCC code[2-1)~2-4)]

2.2.1 Particle calculation method[2-5)~2-6)]

2.2.1.1 Basic equation and solution

In the code used in this study, plasma is calculated using the particle method. Plasma modeling can be broadly divided into particle models and electromagnetic fluid models. However, the fluid model cannot handle the electron energy distribution function and cannot simulate the sheath. In the thruster treated in this study, the potential difference formed by the sheath between the thruster and the wall surface of the thruster is very important in calculating the potential difference formed inside and outside the thruster. Therefore, the fluid model was not adopted and the particle model was adopted. The basic equation in particle calculation is the equation of motion of charged particles (electrons in this calculation) shown below.

$$m\frac{d\boldsymbol{v}}{dt} = q(\boldsymbol{E} + \boldsymbol{v} \times \boldsymbol{B}) \tag{2-1}$$

$$\frac{d\boldsymbol{x}}{dt} = \boldsymbol{v} \tag{2-2}$$

Here, m represents the mass of the particle, v represents the velocity of the particle, x represents the location of the particle, t represents the time, q represents the charge of the particle, E represents the electric field, B represents the magnetic field flux density. The motion of the particle is calculated by solving this equation of motion. If equation. (2-2) is differentiated by using the leap frog method,

$$\frac{\boldsymbol{x}^{n+1} - \boldsymbol{x}^{n}}{\Delta t} = \boldsymbol{v}^{n+1/2} \tag{2-3}$$

equation. (2-3) could be obtained. The superscript of each variable in the formula represents the time. With the one-time step calculation proceeded, the value increases by one. If the time center difference is applied to equation. (2-3),

$$\frac{\boldsymbol{v}^{n+1/2} - \boldsymbol{v}^{n-1/2}}{\Delta t} = \frac{q}{m}\left\{\boldsymbol{E}^{n} + \frac{1}{2}(\boldsymbol{v}^{n+1/2} + \boldsymbol{v}^{n-1/2}) \times \boldsymbol{B}^{n}\right\} \tag{2-4}$$

equation(2-4) could be obtained. The superscript $n-1/2$ means that the value is the time before a certain time n by $\Delta t/2$ steps. Similarly, $n+1/2$ means that the value is the time advanced by $\Delta t/2$ steps from a certain time n.

To calculate the motion of a charged particle, solve equation. (2-4) for $\boldsymbol{v}^{n+1}$ and substitute $\boldsymbol{v}^{n+1}$ for equation. (2-3), the position $\boldsymbol{x}^{n+1}$ of the new particle can be obtained. If equation. (2-4) is transformed into a form using a matrix,

$$\boldsymbol{A}\boldsymbol{v}^{n+1/2} = \boldsymbol{S} \tag{2-5}$$

it can be expressed as equation. (2-5). Here, $\alpha \cdot \beta \cdot \gamma \cdot \delta$ are defined as follows.

$$\alpha = \frac{q\Delta t}{2m} B_x^n \tag{2-6}$$

$$\beta = \frac{q\Delta t}{2m} B_y^n \tag{2-7}$$

$$\gamma = \frac{q\Delta t}{2m} B_z^n \tag{2-8}$$

$$\delta = 1 + \alpha^2 + \beta^2 + \gamma^2 \tag{2-9}$$

Here, ***E*** and ***B*** represent the respective values at each particle position, so it is necessary to interpolate and obtain them by the PIC method described later. Using these, the matrix ***A*** and the vector ***S*** can be expressed as follows.

$$\boldsymbol{A} = \begin{pmatrix} 1 & -\gamma & \beta \\ \gamma & 1 & -\alpha \\ -\beta & \alpha & 1 \end{pmatrix} \tag{2-10}$$

$$\boldsymbol{S} = \begin{pmatrix} v_x^m + cE_x^n + \gamma_y^m - \beta v_z^m \\ v_y^m + cE_y^n + \alpha_y^m - \gamma v_z^m \\ v_z^m + cE_z^n + \beta_y^m - \alpha v_z^m \end{pmatrix} \tag{2-11}$$

Here, $c = q\Delta t/m$ and $m = n - 1/2$. Furthermore, the inverse matrix of ***A*** can be applied to both sides of Eq. (5-5) from the left and transformed as follows to obtain the velocity $\boldsymbol{v}^{n+1/2}$.

$$\boldsymbol{v}^{n+1/2} = \boldsymbol{A}^{-1}\boldsymbol{S} \tag{2-12}$$

$$\boldsymbol{A}^{-1} = \frac{1}{\delta}\begin{pmatrix} 1+\alpha^2 & \alpha\beta+\gamma & \alpha\gamma-\beta \\ \alpha\beta-\gamma & 1+\beta^2 & \beta\gamma+\alpha \\ \alpha\gamma+\beta & \beta\gamma-\alpha & 1+\gamma^2 \end{pmatrix} \tag{2-13}$$

2.2.1.2 Super particle

In the particle simulation method, the basic equations are solved for each particle, but in the microwave discharge ion engine processed in this calculation, each 1 m^3 contains 10^{17} to 10^{18} particles, but the number of particles that our computing system can hold is only on the order of 10^{12}. Even with the latest supercomputers, it is impossible to process all the particles one by one, and it wastes memory and increases the computational cost. Therefore, as particles processed in particle simulations, we use super particle to combine the charge and mass of many particles into one, while keeping the charge-to-mass ratio of the actual particles constant. The smaller the number of particles contained in this number of super particle, the less noise, but the higher the computational cost, which is a cost-accuracy

trade-off. The number of super particles is usually determined based on the number of particles contained in 1 cell being 10 or more and the weight of super particles is smaller than the number of particles to be processed (from statistical properties). As one of the criteria for the study this time, a cell should contain 100 or more particles.

2.2.1.3 Mesh size

The mesh size in the particle method is different from fluid calculation such as CFD, and the grid formation method itself does not affect the accuracy of the analysis, and it depends on whether the target physical phenomenon can be reproduced. First, the mesh size for the physical phenomenon to be analyzed is determined from the following Debye length, etc., and the time step is determined from the constraints of the scheme that comes from the mesh size. The mesh size Δ used in the calculation is calculated from the electron temperature T_e, the Boltzmann constant k_b, and the electron density n_e.

Debye length λ_{De} is:

$$\lambda_{De} = \sqrt{\frac{\varepsilon_0 k_b T_e}{n_e e^2}} \tag{2-12}$$

which is desirable to be:

$$\Delta \leq \lambda_{De} \tag{2-13}$$

Moreover, plasma frequency ω_{pe} is:

$$\omega_{pe} = \sqrt{\frac{n_e e^2}{m_e \varepsilon_0}} \tag{2-14}$$

So the condition for the absence of numerical instability is:

$$\Delta t \leq \omega_{pe}^{-1} \tag{2-15}$$

Considering the accuracy of time integration, the condition usually used is:

$$\Delta t \leq 0.2\omega_{pe}^{-1} \tag{2-16}$$

Furthermore, the electron cyclotron frequency is:

$$\omega_c = \frac{eB}{m_e} \tag{2-17}$$

In order to simulate the phenomena associated with the whirling motion of charged particles in a magnetic field, the time step is required to satisfy:

$$\Delta t << \omega_c^{-1} \tag{2-18}$$

In addition, there is a constraint that particles must not jump over one cell or more at every

time period. In particular, this condition is indispensable for charged particles because the electromagnetic force specified for each lattice works. This is called the Courant condition. In three dimensions, the time step Δt must satisfy:

$$\Delta t \leq \frac{1}{v\sqrt{\frac{1}{(\Delta x)^2}+\frac{1}{(\Delta y)^2}+\frac{1}{(\Delta z)^2}}} \tag{2-19}$$

This condition is extremely strict, and the calculation becomes unstable if it is not satisfied even a little. In reality, about 1/10 of this is desirable. Here, v is the maximum thermal velocity of the particle or the electromagnetic wave velocity, that is, the speed of light. Since the conditions are different between FDTD-PIC and Full-PIC, it will be explained in the calculation conditions of each model.

2.2.1.4 PIC method

The position of each particle exists in the calculation area with a fineness corresponding to the accuracy of the variable. On the other hand, the amount of field (charge density and electric field calculated using his FDTD method described later) is spatially differentiated and calculated, so it is defined on a computational grid called a mesh. This mesh size is the spatial resolution of the field quantity. Therefore, it is necessary to interpolate the amount of field defined on these meshes at the positions of each particle, and conversely, distribute the particle information on the mesh. At that time, a method called Particle-In-Cell (PIC) is used. The details are shown below.

First, the cell number (i,j,k) to which the particle belongs is obtained from the position of the particle. Next, find the distances $dx1$, $dx2$, $dy1$, $dy2$, $dz1$, $dz2$ on each coordinate axis between the particles and the grid points shown in Fig.2-2. Using these values, the volumes of the rectangular parallelepipeds V_1~V_8 shown in the figure are obtained. Then, the amount of the field felt by the particles is interpolated using the volume ratio of this rectangular parallelepiped. As will be described later, the electromagnetic field calculated by the FDTD method is defined at a position deviated by half a cell from the lattice point. Figure 2-2 shows the case of interpolating the values defined on the grid points (only the static magnetic field in this calculation) or the case of distributing the values(current density in this calculation)on the grid points. Therefore, when interpolating the electric field calculated by the FDTD method, it is necessary to calculate the volume of each rectangular parallelepiped in consideration of the deviation of half a cell. Next, a specific

calculation procedure will be described using a static magnetic field as an example.

Assuming that the static magnetic field $B(x,y,z)$ induced by the particle at coordinates (x, y, z) is V for the cell volume, as shown in the figure for the cube divided by the particles, naming in turn V_1 to V_8, the weight of each lattice point is:

$$A_n = \frac{V_n}{V}(n = 1 \sim 8) \tag{2-20}$$

and the static magnetic field induced by the particle is:

$$\begin{aligned} B(x,y,z) = {} & A_1 B(i,j,k) + A_2 B(i+1,j,k) \\ & + A_3 B(i+1,j,k+1) + A_4 B(i,j,k+1) \\ & + A_5 B(i,j+1,k) + A_6 B(i+1,j+1,k) \\ & + A_7 B(i+1,j+1,k+1) + A_8 B(i,j+1,k+1) \end{aligned} \tag{2-21}$$

Next, the case of distributing the charge density and the current density to the grid points will be described. The charge density is defined on the grid points of the cell shown in Fig. 2-2, and when there is one superparticle representing N particles in the cell, the charge density assigned on the grid points is

$$\rho(i,j,k) = \frac{V_1}{V^2} qN \tag{2-22}$$

The charge density on the grid points can be obtained by summing all the particles. Also, since when charged particles of charge q are flowing at the condition of density n, velocity $\boldsymbol{v}$, the current density is

$$\boldsymbol{j} = qn\boldsymbol{v} \tag{2-23}$$

with this:

$$\boldsymbol{j}(i,j,k) = \frac{V_1}{V^2} qN\boldsymbol{v} \tag{2-24}$$

equation. (2-24) could be obtained.

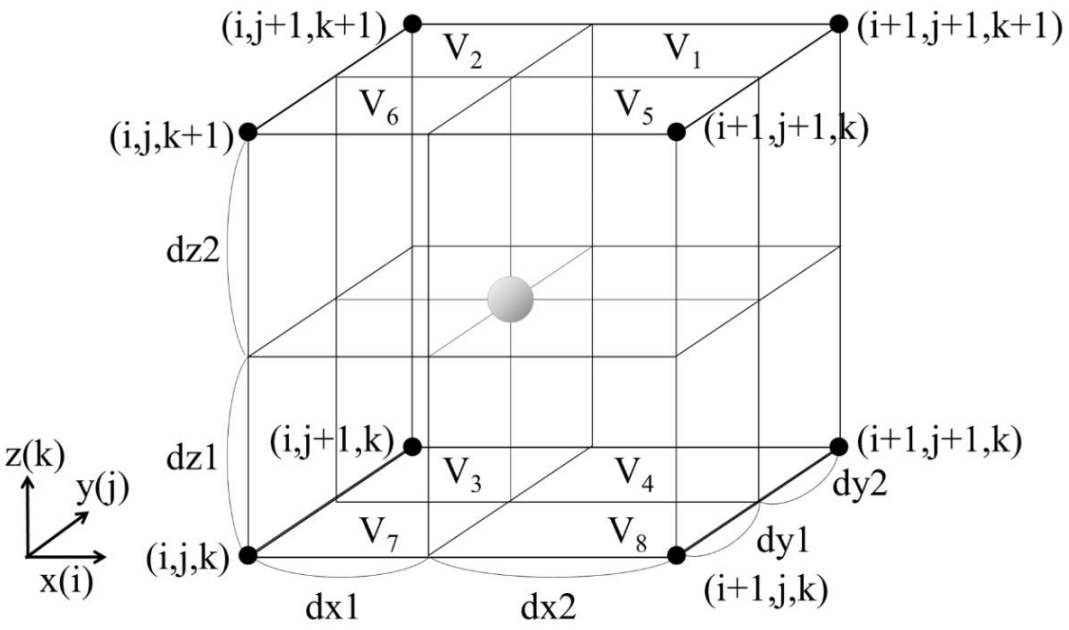

Fig. 2-2 Schematics of 3D-PIC method

2.2.1.5 Particle boundary condition

When the plasma and the conductor wall contact each other, a sheath with a thickness several times the Debye length is formed on the conductor surface. In this region, a potential difference is formed such that the fluxes of electrons and ions flowing into the conductor are equal. The ions are accelerated by this potential difference and the electrons are slowed down or repelled. Since FDTD-PIC-MCC does not take into account the effect of electrostatic fields, it is necessary to assume reflections due to the sheath potential of electrons. The sheath potential can be analyzed by Full-PIC-MCC, but the effect of the potential distribution cannot be coupled so far. Therefore, 20V was set based on the experimental value and the results of previous numerical analysis, and when reaching the wall surface, more than 20eV disappeared uniformly and reflected more.

2.2.1.6 Collision calculation MCC method

In this numerical analysis code, the MCC (Monte-Carlo-Collision) method is used for the analysis of particle collisions. The Monte Carlo collision method is to determine the collision between particles using the probability of determining from the collision frequency between each particle and a random number. It will be described in detail below.

➢ Collision type

In the code currently in use, charged particles move under the influence of an

electromagnetic field and collide with neutral particles. Although plasma consists of electrons, ions and neutral particles, since the number density of electrons and ions is much smaller than that of neutral particles, each electron-electron, electron-ion, and ion-ion collision can be ignored, and only electron-neutral collisions are handled. Currently only elastic, excited and ionizing collisions are assumed to be handled as collision types.

➢ Mean free path and transmittance

Consider a plate of thickness l and the number density of constituent substances N. Suppose a beam of particles with energy E hits the surface of the plate vertically α. When the incident particles collide with the material that makes up the plate, some of the particles scatter and deviate. Because of this, the number of particles penetrating the plate without any collisions at all will be smaller than the number of incident particles. If σ is the cross section of the collision and n is the number of particles passing through the collision point, the number of particles dn in the differential fraction reduced when passing through the tiny thickness dl can be expressed as:

$$dn = -nN\sigma dl \tag{2-25}$$

By integrating equation. 2-25, the number of particles that pass through the plate without colliding is obtained as:

$$n = n_0 exp(-N\sigma l) \tag{2-26}$$

Here, n_0 represents the number of particles passing through the surface(l=0) of the plate. Therefore, the probability of the first collision between the distance (l, $l + dl$) is

$$P_{initial}(l)dl = exp(-N\sigma l)N\sigma dl \tag{2-27}$$

The probability of a collision along distance l is

$$\begin{aligned} P(l) &= \int_0^l Pinitial(l)dl \\ &= 1 - exp(-N\sigma l) \end{aligned} \tag{2-28}$$

The average distance λ that the particles move before the first collision is expressed as follows using $P(l)$.

$$\begin{aligned} \lambda &= \int_0^\infty lP(l)dl \\ &= \frac{1}{N\sigma} \end{aligned} \tag{2-29}$$

This is called the mean free path. Therefore, in order to determine the distance from an arbitrary point to the first collision in the calculation in the Monte Carlo method, the random number r can be used and set to:

$$\begin{aligned} r &= P(l) \\ &= 1 - exp\ (-\frac{1}{\lambda}) \end{aligned} \tag{2-30}$$

Further, when this is transformed, it becomes:

$$l = -\lambda \ln(l - r) \tag{2-31}$$

Here, r is a uniform random number, so if l-r is replaced with r, it is expressed as:

$$l = -\lambda \ln(r) \tag{2-32}$$

Also, if the cross section area when a particle of speed v collides with a neutral particle is σ, the number of times this particle collides with a neutral particle per second, that is, the collision frequency υ, could be expressed by using equation. (2-28) as:

$$\begin{aligned} \upsilon &= \frac{v}{\lambda} \\ &= \sigma N v \end{aligned} \tag{2-31}$$

➢ Collision probability / collision determination

The cross section area of every collision is expressed as a function of the energy of the charged particles.

$$\sigma = \sigma(E) \tag{2-32}$$

Therefore, if the charged particle velocity is known, the collision frequency of the charged particle and the neutral particle for each collision type can be calculated. The sum of the collision frequencies of all collision types is called the total collision frequency υ_{total}. Therefore, the collision probability $P_{\text{collision,m}}$ of a certain charged particle m can be expressed by the following equation using equation. (2-28).

$$\upsilon_{total} = \mathrm{n}_{gas} \sigma_{total} \mathrm{v}_m \tag{2-33}$$

$$P_{\text{collision,m}} = 1 - \exp(-N\sigma l) N\sigma dl \tag{2-34}$$

Here, n_{gas} represents the number density of neutral particle, v_{m} represents the velocity of charged particle m, σ_{total} represents the total cross section area. By using a random number r_1 ($0 < \mathrm{r}_1 < 1$), when $P_{\text{collision,m}} > \mathrm{r}_1$, particle m is assumed to collide during the time step Δt.

➢ Collision type determination

Since $P_{\text{collision,m}}$ in the previous section is a value that includes all collision types, if it is decided that a collision will occur, it is necessary to determine which type of collision will occur next.

$$0 \le r_2 \le \frac{\sigma_{elastic}}{\sigma_{total}} \quad \text{(Elastic collision)}$$

$$\frac{\sigma_{elastic}}{\sigma_{total}} \le r_2 \le \frac{\sigma_{elastic} + \sigma_{excitation}}{\sigma_{total}} \quad \text{(Excitation collision)}$$

$$\frac{\sigma_{elastic} + \sigma_{excitation}}{\sigma_{total}} \le r_2 \le \frac{\sigma_{elastic} + \sigma_{excitation} + \sigma_{ionization1}}{\sigma_{total}} \quad \text{(First ionization collision)}$$

$$\frac{\sigma_{elastic} + \sigma_{excitation} + \sigma_{ionization1}}{\sigma_{total}} \le r_2 \le \frac{\sigma_{elastic} + \sigma_{excitation} + \sigma_{ionization1} + \sigma_{ionization2}}{\sigma_{total}}$$

(Second ionization collision)

Here, equation $\sigma_{total} = \sigma_{elastic} + \sigma_{excitation} + \sigma_{ionization1} + \sigma_{ionization2}$ could be obtained. In this way, the cross section area ratio and the random number are correlated to determine the type of collision. In this numerical calculation, the propellants are the xenon and argon gases used in the experiment. Figure 2-3 shows the cross section area data for the xenon gas used in this calculation. Figure 2-4 shows the cross section area data for the argon gas used in this calculation. Cross section area data were mostly obtained by fitting to the National Institute of Fusion Science (NIFS) database.[2-7] In order to complete the data of secondary ionization, the data of D. Mathur and H. Straub et al.[2-8)~2-9)] were used under the premise of confirming the correlation with the existing data. The fitting method is to fit different functions in each energy interval to achieve a more accurate fit. Considering that more than triple ionization has little effect on the collision calculation, only first ionization and second ionization are considered in this calculation.

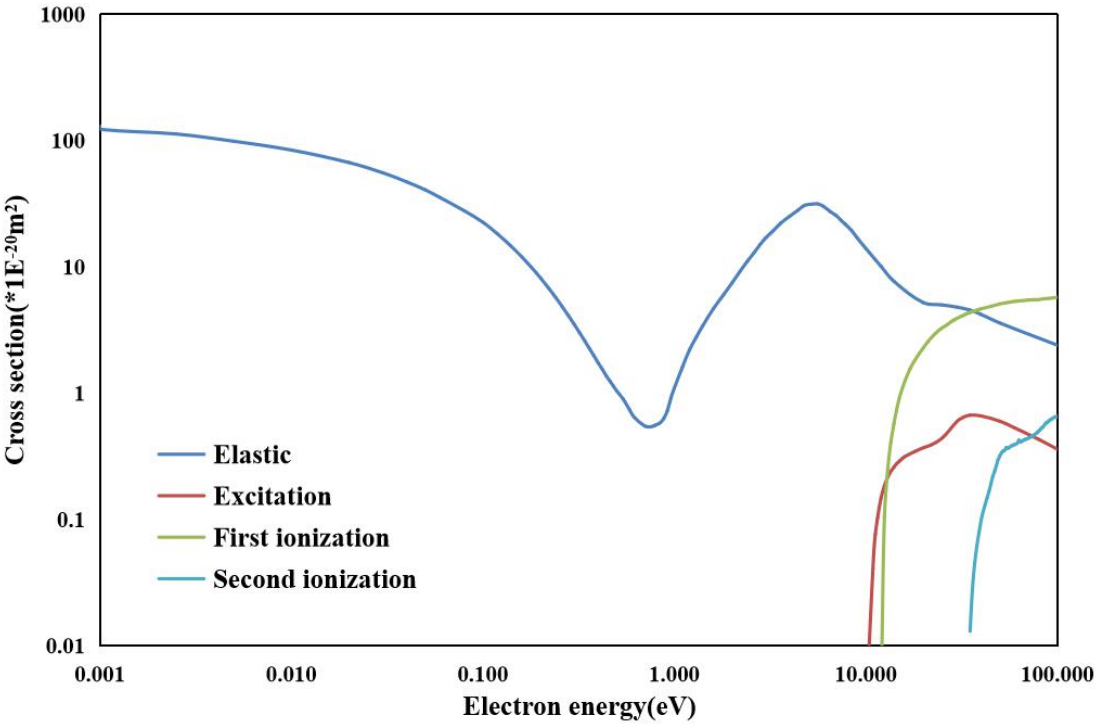

Fig. 2-3 Cross section of xenon

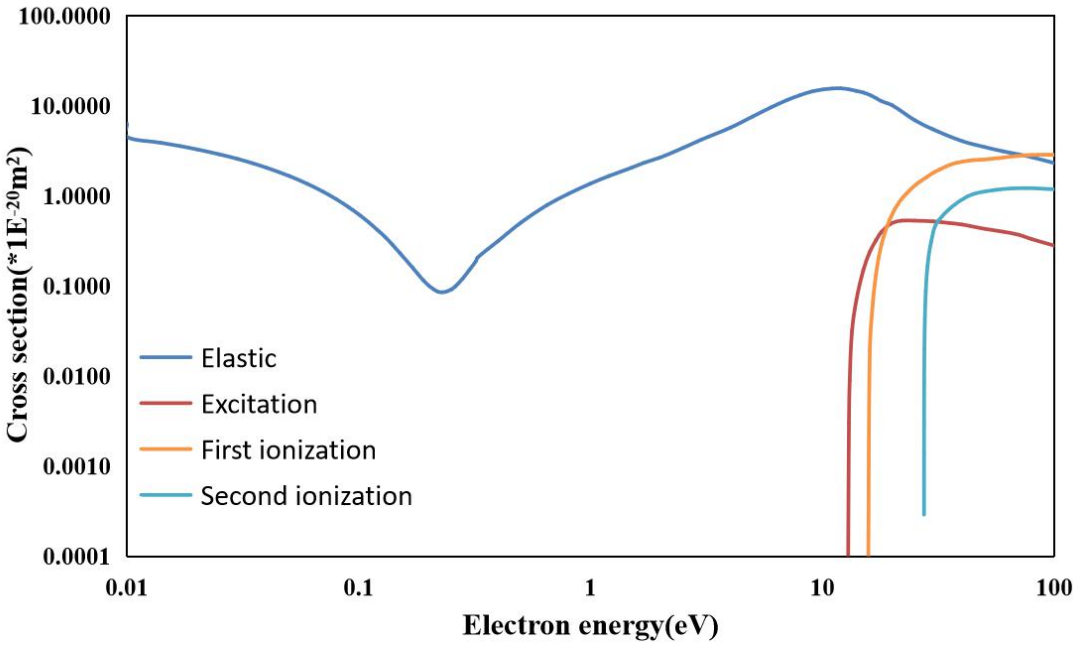

Fig. 2-4 Cross section of argon

➢ Post-collision energy and scattering angle

The particles transfer energy before and after the collision and are scattered in a different direction than before the collision. The calculation method of energy and scattering angle in each collision is described below.

(1)Elastic collision

If the velocity ($\boldsymbol{v}_1$,$\boldsymbol{v}_2$) of a pair of particles becomes ($\boldsymbol{v}`_1$,$\boldsymbol{v}`_2$) after collision, it could be expressed as:

$$\boldsymbol{v}_1' = \frac{1}{2}(\boldsymbol{v}_1 + \boldsymbol{v}_2 - \boldsymbol{u}') \tag{2-35}$$

$$\boldsymbol{v}_2' = \frac{1}{2}(\boldsymbol{v}_1 + \boldsymbol{v}_2 + \boldsymbol{u}') \tag{2-35}$$

Here, $\boldsymbol{u}' = \boldsymbol{v}_2' - \boldsymbol{v}_1'$ represents the relative velocity. One particle is an electron and the other is a neutral particle, and the velocities of the electron and neutral particle before collision are $\boldsymbol{v}_e \cdot \boldsymbol{v}_n$, and the velocities after collision are $\boldsymbol{v}_e' \cdot \boldsymbol{v}_n'$, respectively. In the collision between an electron and a neutral particle, only the electron is scattered because the mass of the electron is much smaller than that of the neutral particle.

Therefore, if the velocity $\boldsymbol{v}_n$ of the neutral particle is ignored, the relative velocity may be $\boldsymbol{u} = \boldsymbol{v}_n - \boldsymbol{v}_e \cong -\boldsymbol{v}_e$. Therefore, if the mass of the electron is *m* and the mass of the neutral particle is *M*, the following equation holds from the energy conservation law of the whole system.

$$\boldsymbol{v}_e' = \frac{m + M\cos\chi}{m + M}\boldsymbol{v}_e + \frac{M\sin\chi}{m + M}\boldsymbol{h} \tag{2-36}$$

Each component in Cartesian coordinates of $\boldsymbol{h}$ is:

$$h_x = v_{er}\cos\phi \tag{2-37}$$

$$h_y = -\frac{v_{ex}v_{ey}\cos\phi - v_e v_{ez}\sin\phi}{v_{er}} \tag{2-38}$$

$$h_z = -\frac{v_{ex}v_{ez}\cos\varphi - v_e v_{ey}\sin\varphi}{v_{er}} \tag{2-39}$$

besides,

$$v_{er} = \sqrt{v_{ey}^2 + v_{ez}^2} \tag{2-40}$$

$$v_e = \sqrt{v_{ex}^2 + v_{ey}^2 + v_{ez}^2} \tag{2-41}$$

χ is the scattering angle and ϕ is an arbitrary angle. Note that the electron velocities given in the equation are after energy loss.

Next, consider the energy balance before and after the collision. If the energy of the electron before the collision is $E_{incident,e}$ and the energy of the electron after the collision is $E_{scattered,e}$, it can be expressed as:

$$E_{scattered,e} = E_{incident,e} \tag{2-42}$$

Electrons tend to be isotropically scattered when the energy $E_{incident,e}$ is small, and mainly forward-scattered when the energy is large. The probability density function of the scattering angle χ in consideration of this is shown below as $g(\chi)$. The unit of $E_{incident,e}$ is eV here.

$$g(\chi) = \frac{E_{incident,e} sin\chi}{2\left\{1 + E_{incident,e} sin^2 \frac{\chi}{2} ln\left|1 + E_{incident,e}\right|\right\}} \qquad (0 \le \chi \le \pi) \tag{2-43}$$

If this is solved, it becomes:

$$cos\chi = 1 + \frac{2\left\{1 - (1 + E_{incident,e})^{r_3}\right\}}{E_{incident,e}} \tag{2-44}$$

By using this value in the equation, the velocity after the collision is obtained. At this time, any angle is given as:

$$\phi = 2\pi r_4 \tag{2-45}$$

(2)Excitation collision

The energy lost by electrons when a neutral particle in the ground state is excited to a certain level is defined as excitation energy $E_{excitation}$, the energy of incident electrons is $E_{incident,e}$, the energy after excitation collision is $E_{scattered,e}$, and the velocity after excitation is $\tilde{\boldsymbol{v}}$. By using these values, the energy balance is expressed as:

$$E_{scattered,e} = E_{incident,e} - E_{excitation} \tag{2-46}$$

and the velocity after excitation is:

$$\tilde{\boldsymbol{v}} = \boldsymbol{v}_e \sqrt{1 - \frac{E_{excitation}}{E_{incident,e}}} \tag{2-47}$$

Here, the excitation collision is divided into the excitation collision and the elastic collision. Then, after losing energy due to excitation, it can be considered that an elastic collision occurs at the velocity of $\tilde{\boldsymbol{v}}$ in equation. (2-47). Substitute $\tilde{\boldsymbol{v}}$ for $\boldsymbol{v}_e$ in equation (2-36) to find the post-collision velocity $\boldsymbol{v}_e'$. Equation. (2-44) is used for the scattering angle at this time, but $E_{scattered,e}$ obtained from equation. (2-46) is used for $E_{incident,e}$ in equation. (2-44). According to the NIFS database, there are six excitation types in argon, and this calculation takes the total cross-sectional area of these excitations as the excitation cross-sectional area. Therefore, the excitation energy $E_{excitation}$ is obtained by taking the weighted average of these six excitation energies with the integral value of each cross

section area as a weight. As a result, the excitation energy was set to 12.96 eV. Similarly, in the case of xenon, the excitation energy is set to 8.34 eV.

(3)Ionization collision

Consider that $E_{incident,e}$ as the energy of incident electrons, $E_{scattered,e}$ is the energy of scattered electrons, $E_{created,e}$ is the energy of electrons generated by ionization, and $E_{ionization}$ is the ionization energy. Using these values, since energy is conserved before and after the collision, the energy balance is expressed as:

$$E_{scattered,e} + E_{created,e} = E_{incident,e} - E_{ionization} \tag{2-48}$$

The energy of the electrons generated by ionization is distributed in the range of 0 ~ ($E_{incident,e}$ − $E_{ionization}$) / 2, but since the energy distribution is unknown, it is assumed that it is uniformly distributed in the range of 0 ~ ($E_{incident,e}$ − $E_{ionization}$) / 2, and is given by the following equation.

$$E_{created,e} = r_5 \frac{(E_{incident,e} - E_{ionization})}{2} \tag{2-49}$$

If the energy lost by the incident electrons due to ionization1 is ΔE, it is expressed as:

$$\Delta E = E_{incident,e} - E_{created,e} \tag{2-50}$$

From equation (2-47), the electron velocity after ionization1 is:

$$\tilde{\boldsymbol{v}} = \boldsymbol{v}_e \sqrt{1 - \frac{\Delta E}{E_{incident,e}}} \tag{2-51}$$

Next, it is considered that particles at this velocity collide elastically. Substitute $\tilde{\boldsymbol{v}}$ for $\boldsymbol{v}_e$ in equation (2-38) to find the post-collision velocity $\boldsymbol{v}_e'$. Equation. (2-44) is used for the scattering angle at this time, but $E_{scattered,e}$ obtained from equation. (2-49) is used for $E_{incident,e}$ in equation. (2-44). The first ionization energy $E_{ionization1}$ is 15.75 eV for argon and 12.13 eV for xenon. The Second ionization energy $E_{ionization2}$ is 27.00 eV for argon and 35.00 eV for xenon.

The energy of the generated electron after ionization is:

$$E_{created,e} = \Delta E - E_{ionization} \tag{2-52}$$

Further, when the velocity $\boldsymbol{v}_e$ of the incident electron is used, the velocity of the generated electron becomes:

$$\boldsymbol{v}_{created,e} = \frac{\boldsymbol{v}_e}{v_e} \sqrt{\frac{2E_{created,e}}{m}} \tag{2-53}$$

Considering that the generated electrons also collide elastically at this velocity, the velocity

after collision can be obtained by substituting $\boldsymbol{v}_{\text{created,e}}$ into equation (2-38) instead of $\boldsymbol{v}_{\text{e}}$. Similarly, the scattering angle is obtained from equation. (2-44) using the energy $E_{\text{created,e}}$ of the generated electrons.

➢ Null-collision method

The Null-collision method is used to reduce the time required for collision calculation. Therefore, a fictitious collision cross section σ_{fake} is introduced. However, it is assumed that it is:

$$\sigma_{fake} < \sigma_{total} \tag{2-54}$$

for all the energy E of the electron. Then, the total collision cross section σ_{total} becomes:

$$\sigma_{total} = \sigma_{elastic} + \sigma_{excitation} + \sigma_{ionization1} + \sigma_{ionization2} + \sigma_{fake} \tag{2-55}$$

Here, if the equation:

$$\sigma_{total} v = \frac{\nu_{collision}}{n_{gas}} = constant \tag{2-56}$$

that satisfied by σ_{fake} is introduced, $\boldsymbol{v}_{\text{collision}}$ becomes constant, that is, $P_{\text{collision,m}}$ becomes constant and does not depend on energy. The collision probability, which has been changed for each particle energy, is treated as constant with the maximum collision probability. Therefore, it is not necessary to calculate $P_{\text{collision,m}}$ for each particle, and it is sufficient to determine the type of collision only for the particles that cause collision without performing collision calculation for all particles. As a result, the calculation time can be significantly reduced.

When the Null-Collision Process is selected, the motion of the particles shall not change at all. Figures 2-5 and 2-6 show the collision frequencies standardized by the neutral particle density of xenon gas / argon gas in the collision of electrons and neutral particles. The value of $\nu_{collision} / n_{gas}$ used in the Null-Collision method in this calculation is argon: 3.92659×10^{-13} m^3 / sec, xenon: 6.46328×10^{-13} m^3 / sec.

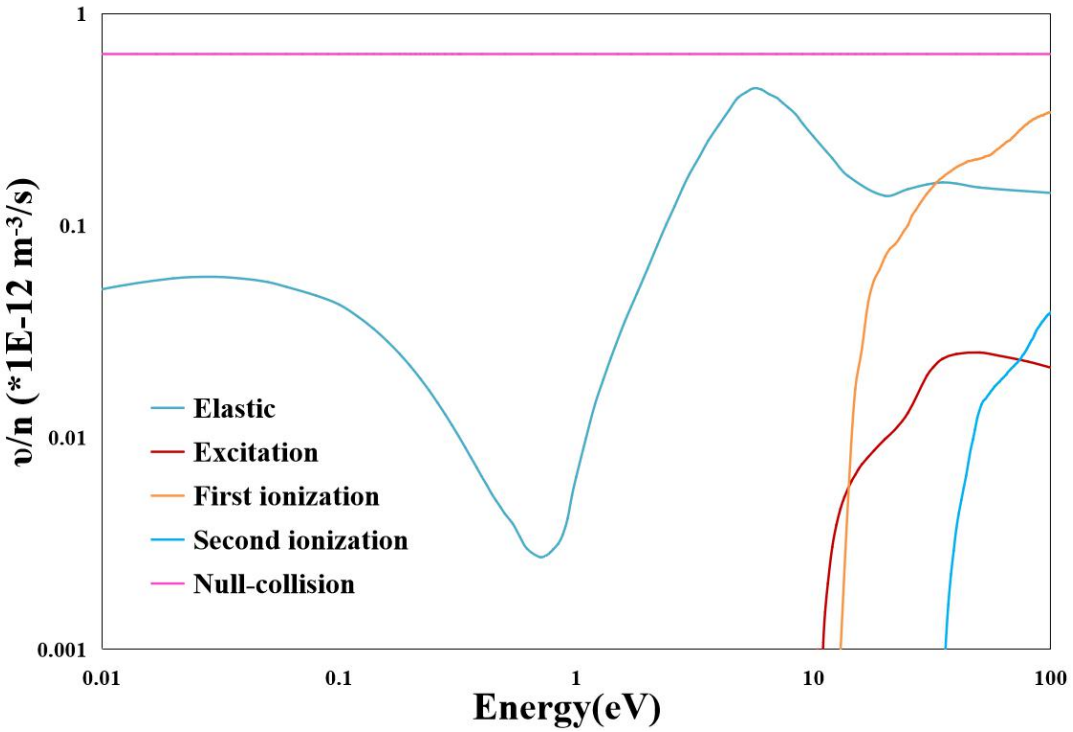

Fig. 2-5 Normalized cross section of xenon

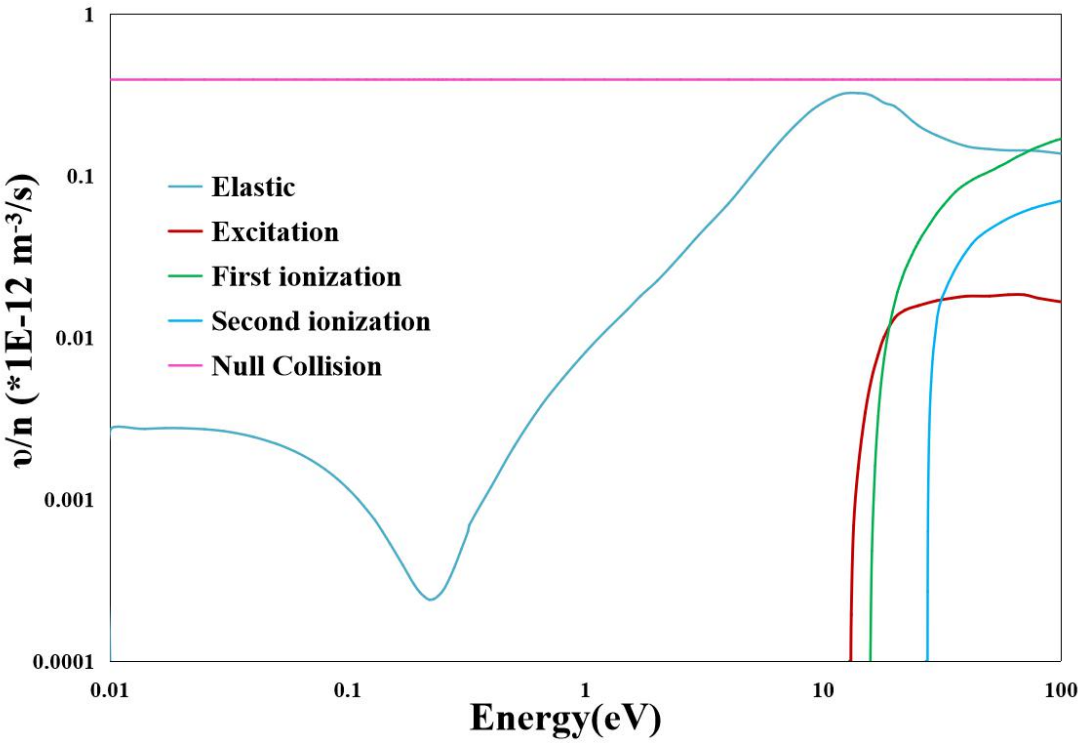

Fig. 2-6 Normalized cross section of argon

➢ Time step constraints

In the Monte Carlo method, one collision for each particle can be processed only once in one time step. However, a time step can contain multiple collisions as long as a limited time step is used. In order to reduce this collision calculation error, it is necessary to make

the time step sufficiently small.

The number of collision misses per time step of a particle is expressed as:

$$r \sim \sum_{k=2}^{\times} P_i^k = \frac{P_i^2}{1-P_i} \tag{2-57}$$

Here, in order to reduce the number of collision mistakes r to 1% or less, it is necessary to set $P_i \le 0.1$. When using null-collision, it is necessary to set the time step so that $P_{null} \le 0.1$, that is, the following equation should be satisfied.

$$\Delta t \le \frac{0.1}{\nu_{null}} \tag{2-58}$$

➢ random number generation

Random numbers are random numbers that are uniformly distributed between (0,1). We avoided using the built-in random number ran() in Fotran, which has a short generation period, and used Mersenne Twister. The period is (219937-1) and the generation rate is fast.

2.2.2 Electromagnetic wave analysis method[2-10)~2-12)]

2.2.2.1 Basic equation

In this calculation, the Finite-difference time-domain method (FDTD method) is used to solve the three-dimensional Maxwell's equations in order to calculate the propagation of electromagnetic waves. Unlike other solutions such as the finite element method and the moment method, the FDTD method is characterized by differentiating Maxwell's equations in the time domain. Therefore, it is possible to calculate the transient time course of electromagnetic wave. Since this calculation code needs to aim at the calculation up to the steady state while combining the electromagnetic wave calculation and the particle calculation, the FDTD method is adopted. The differential form of Maxwell's equations used as the basic equation is shown below.

$$\nabla \times E = -\mu_0 \frac{\partial H}{\partial t} \tag{2-59}$$

$$\nabla \times H = \varepsilon_0 \frac{\partial E}{\partial t} + J \tag{2-60}$$

Here, E represents electric field strength, H represents magnetic field strength, μ_0 represents vacuum permeability, ε_0 represents vacuum permittivity, and J is current density. The calculation is performed by taking the temporal and spatial differences of this equation.

2.2.2.2 Difference equation

In the three-dimensional FDTD method, the electric and magnetic fields are arranged on the cell as shown in Fig. 2-7, both electric and magnetic fields are spatially alternately arranged, the electric field is defined along each side of the cell, and the magnetic field is defined in the center of the cell surface.

Proposed by Yee, it is arranged to satisfy Maxwell's equations that the curl of the induced electric field($\nabla \times E$) is equal to the rate of change of the magnetic induction and the curl of the induced magnetic field($\nabla \times H$) is equal to the sum of the current density and the rate of change of the electric field strength.

Based on the arrangement of this electromagnetic field, equations (2-59) and (2-60) are shown in equations ((2-61) to (2-62)) with the center difference between space and time. Here, $\Delta x, \Delta y, \Delta z$ is the space width, Δt is the time width, subscript (i, j, k) is the coordinate in the cell, subscript n is the time step.

$$H_x^{n+\frac{1}{2}}(i, j+1/2, k+1/2) = H_x^{n-\frac{1}{2}}(i, j+1/2, k+1/2) + \frac{\Delta t}{\mu_0(i, j+1/2, k+1/2)} \left\{ \frac{E_y^n(i, j+1/2, k+1) - E_y^n(i, j+1/2, k)}{\Delta z} + \frac{E_z^n(i, j, k+1/2) - E_z^n(i, j+1, k+1/2)}{\Delta y} \right\} \tag{2-61}$$

$$H_y^{n+\frac{1}{2}}(i+1/2, j, k+1/2) = H_y^{n-\frac{1}{2}}(i+1/2, j, k+1/2) + \frac{\Delta t}{\mu_0(i+1/2, j, k+1/2)} \left\{ \frac{E_z^n(i+1, j, k+1/2) - E_z^n(i, j, k+1/2)}{\Delta x} + \frac{E_x^n(i+1/2, j, k) - E_x^n(i+1/2, j, k+1)}{\Delta z} \right\} \tag{2-62}$$

$$H_z^{n+\frac{1}{2}}(i+1/2, j+1/2, k) = H_z^{n-\frac{1}{2}}(i+1/2, j+1/2, k) + \frac{\Delta t}{\mu_0(i+1/2, j+1/2, k)} \left\{ \frac{E_x^n(i+1/2, j+1, k) - E_x^n(i+1/2, j, k)}{\Delta y} + \frac{E_y^n(i, j+1/2, k) - E_y^n(i+1, j+1/2, k)}{\Delta x} \right\} \tag{2-63}$$

$$E_x^{n+1}(i+1/2,j,k)=E_x^n(i+1/2,j,k)+\frac{\Delta t}{\varepsilon_0(i+1/2,j,k)}$$
$$\left\{\frac{H_z^{n+\frac{1}{2}}(i+1/2,j+1/2,k)-H_z^{n+\frac{1}{2}}(i+1/2,j-1/2,k)}{\Delta y}\right.$$
$$\left.+\frac{H_y^{n+\frac{1}{2}}(i+1/2,j,k-1/2)-H_y^{n+\frac{1}{2}}(i+1/2,j,k+1/2)}{\Delta z}-J_x(i+1/2,j,k)\right\} \tag{2-64}$$

$$E_y^{n+1}(i,j+1/2,k)=E_y^n(i,j+1/2,k)+\frac{\Delta t}{\varepsilon_0(i,j+1/2,k)}$$
$$\left\{\frac{H_x^{n+\frac{1}{2}}(i,j+1/2,k+1/2)-H_x^{n+\frac{1}{2}}(i+1/2,j+1/2,k-1/2)}{\Delta z}\right.$$
$$\left.+\frac{H_z^{n+\frac{1}{2}}(i-1/2,j+1/2,k)-H_z^{n+\frac{1}{2}}(i+1/2,j+1/2,k)}{\Delta x}-J_x(i,j+1/2,k)\right\} \tag{2-65}$$

$$E_z^{n+1}(i,j,k+1/2)=E_z^n(i,j,k+1/2)+\frac{\Delta t}{\varepsilon_0(i,j,k+1/2)}$$
$$\left\{\frac{H_y^{n+\frac{1}{2}}(i+1/2,j,k+1/2)-H_y^{n+\frac{1}{2}}(i-1/2,j,k+1/2)}{\Delta x}\right.$$
$$\left.+\frac{H_x^{n+\frac{1}{2}}(i,j-1/2,k+1/2)-H_x^{n+\frac{1}{2}}(i,j+1/2,k+1/2)}{\Delta y}-J_x(i,j,k+1/2)\right\} \tag{2-66}$$

From equations ((2-61) to (2-66)), the magnetic field strength $H^{n+\frac{1}{2}}$ at time step $\mathrm{n}+1/2$ can be obtained by the electric field strength E^n before half time step and the magnetic field strength $H^{n-\frac{1}{2}}$ before one time step, and the electric field strength E^{n+1} at time step $\mathrm{n}+1$ can be obtained from the magnetic field strength $H^{n+\frac{1}{2}}$ before half time step and the electric field strength E^n before one time step.

All the initial values are 0 and the electric field is applied only between the antenna and the central yoke. J in the equation is the current density obtained from particle calculation, and this term means the effect of charged particles on electromagnetic wave.

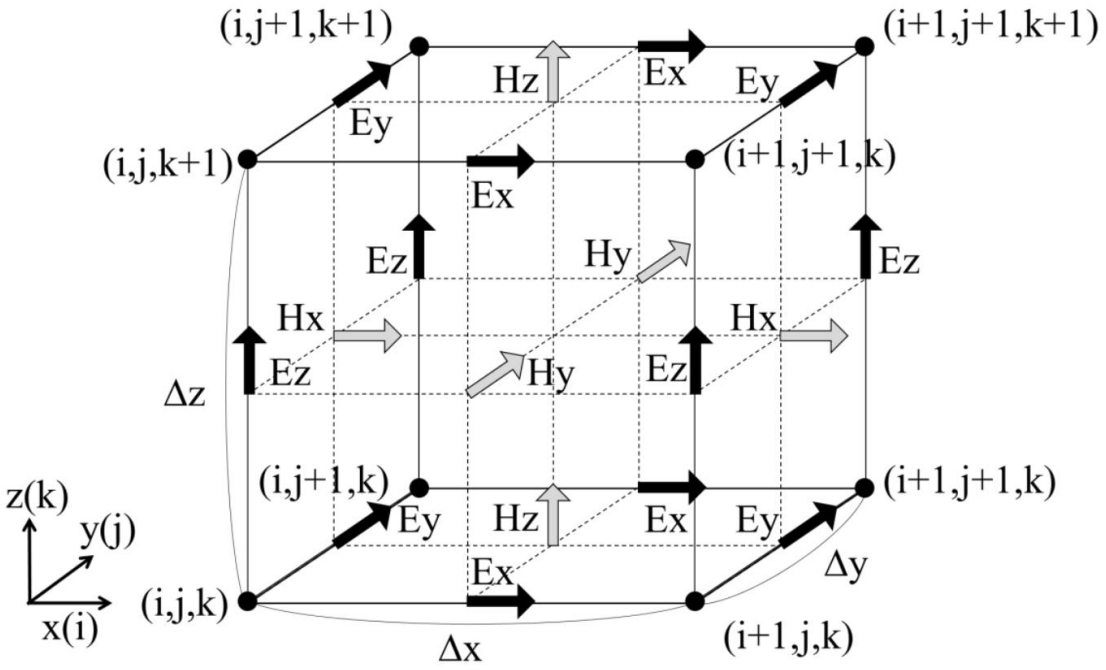

Fig. 2-7 Schematics of FDTD method.

2.2.2.3 Antenna simulation and power supply method[2-13)~2-14)]

In this calculation, the antenna is treated as a perfect conductor. Microwave power supply is simulated by applying an electric field to the coaxial cable part inside the central yoke. Figure 2-8 shows the cross section of the feeding surface inside the central yoke. This figure shows the case where the mesh size is 0.50 mm. The antenna has a diameter of 1 mm and the inner diameter of the central yoke is 3.00 mm. The cells shown in gray in the figure are conductors, and the cells shown in white are the cells in which electromagnetic waves propagate freely in space. The electric field strength to be applied to this space was determined from the following formula.

$$E_r = \frac{V_0}{r} \tag{2-67}$$

$$E_x = E_r \cos\theta \tag{2-68}$$

$$E_y = E_r \sin\theta \tag{2-69}$$

Here, V_0 is the voltage between the antenna and the central yoke, r is the distance from the central axis of the antenna, and θ is the angle formed by each feeding electric field and the x axis with the antenna central axis as the origin. V_0 was determined based on the poynting vector passing through the central yoke.

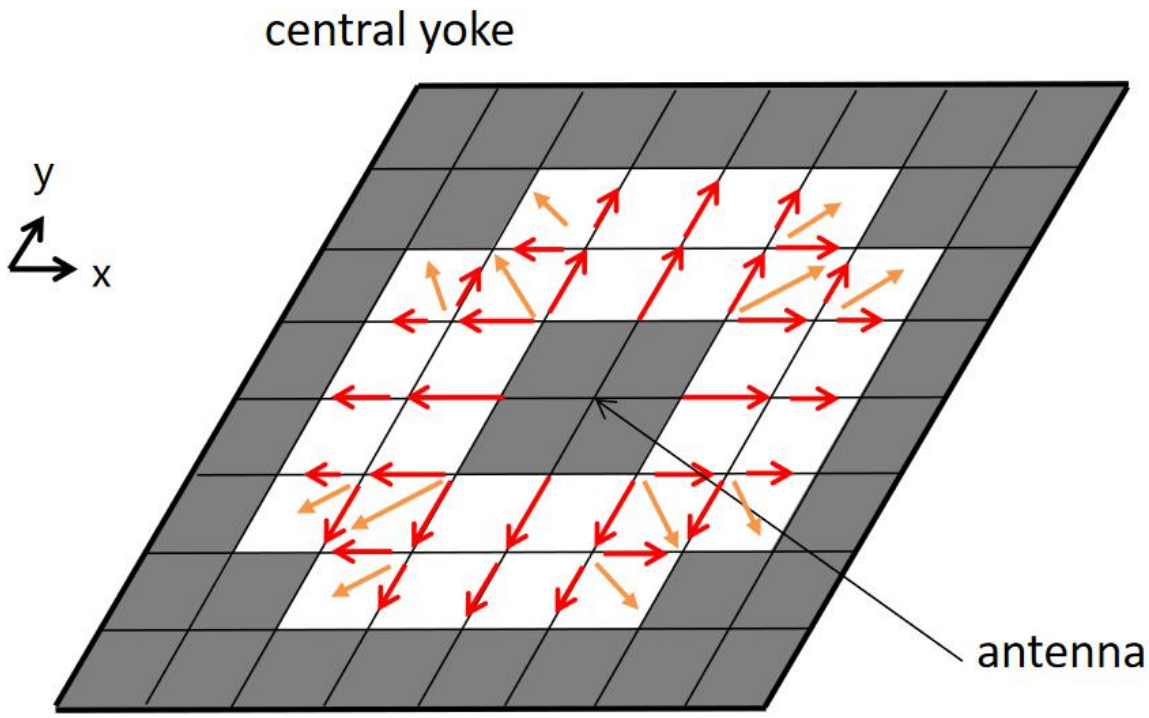

Fig. 2-8 Cross section of microwave feeding point

2.2.2.4 Measurement of input energy

The input energy is calculated by calculating the pointing vector in the central yoke. The pointing vector S is expressed by the following equation and represents the energy flow of electromagnetic waves.

$$S = E \times H \tag{2-70}$$

As a basic property of electromagnetic waves, when the impedance of the propagation path changes, a part of the wave is reflected at that point. This wave is called a reflected wave, and when a microwave is injected into the thruster, a part of the input is radiated from the antenna and absorbed by electrons, but a part is returned as a reflected wave. Only the net input power after deducting the reflected wave can be calculated only by calculating the poynting vector on one side. However, in the actual experiment, the input wave power is a control parameter, and it is necessary to calculate this value even in numerical calculation. Therefore, as shown in Fig. 2-9, the pointing vector was calculated

on two planes. When an electric field is applied to the surface represented by the green line, input waves with the same energy propagate on both sides of the electric field. The wave propagating to the tip of the antenna is radiated into the discharge chamber and absorbed by electrons, but part of it is returned as a reflected wave. Then, the reflected wave reaches the root of the antenna and is absorbed under Mur's first absorption boundary condition (described later). Therefore, on the antenna side from the electric field input point, the traveling directions of the input wave (FWD) and the reflected wave (REF) are opposite, and the poynting vector is the value S_1 where these waves cancel each other out. On the other hand, the directions of the input wave and the reflected wave are aligned on the back yoke side of the electric field input point, and the poynting vector is a value S_2 in which these are strengthened. Therefore, the input wave poynting vector S_{fwd} and the reflected wave poynting vector S_{ref} are expressed as follows.

$$S_{fwd} = \frac{S_1 + S_2}{2} \tag{2-71}$$

$$S_{ref} = \frac{-S_1 + S_2}{2} \tag{2-72}$$

The value of this S_{fwd} was treated as the input power, and the voltage between the antenna and the central yoke was determined so that this value became the target value. The voltage was kept constant during the calculation of the 3D-FDTD-PIC code.

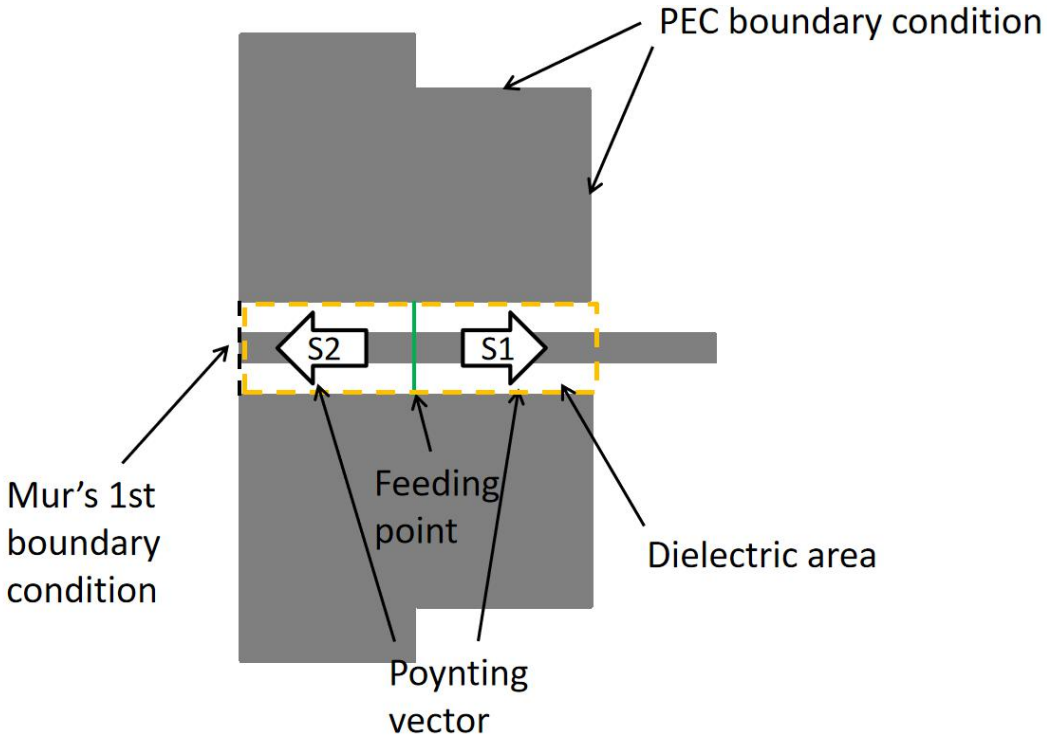

Fig. 2-9 Calculation of microwave feeding power(Y-Z plane)

2.2.2.5 PEC (Perfect Electric Conductor) boundary conditions

Aluminum, molybdenum, and soft iron that make up the thruster are all regarded as a perfect conductor, and the PEC boundary condition with the electric field component parallel to the boundary as 0 is used. However, there is an electric field perpendicular to the interface.

2.2.2.6 Mur absorption boundary condition[2-15)]

In the calculation using the FDTD method, it is necessary to set some boundary conditions at the end of the calculation area and close the calculation area. Then, in order to simulate an open region, an absorbing boundary condition is arranged. There are several types of absorbing boundary conditions, but among them, Mur's first absorbing boundary condition, which is easy to implement and uses a small amount of memory, was used. Details will be described below.

It is assumed that a plane wave having an E_z component is incident on the absorbing boundary of $x = 0$ from the positive direction of x. Assuming that the propagation velocity is v, the wave traveling in the negative direction of x is expressed as

$$E_z = E_z(x + vt) \tag{2-73}$$

which satisfies the following differential equation.

$$\frac{\partial E_z}{\partial x} - \frac{1}{v}\frac{\partial E_z}{\partial t} = 0 \tag{2-74}$$

If there is no reflection at the boundary of $x = 0$, the electric field should propagate with satisfaction in equation. (2-73). That is, equation. (2-74) is satisfied even at the boundary. In order to formulate this in the form of the FDTD method, if equation (2-74) is differentiated with respect to time:

$$\begin{aligned} \frac{\partial E_z}{\partial t} &= \frac{E_z^n - E_z^{n-1}}{\Delta t} \\ &= v\frac{\partial E_z^{n-\frac{1}{2}}}{\partial x} \end{aligned} \tag{2-75}$$

Here, the differentiation for x on the right side is performed with $x = 1/2$ because the electric field is assigned to $x = 0, \Delta x$, and is substituted into equation. (2-74).

$$\frac{E_r^n(i, n-1/2) - E_r^{n-1}(i, n-1/2)}{\Delta t} = v\frac{E_r^{n-\frac{1}{2}}(i, n) - E_r^{n-\frac{1}{2}}(i, n-1)}{\Delta z} \tag{2-76}$$

However, the $E_z^n(1/2)$, $E_z^{n-1}(1/2)$ in the equation. (2-75) couldn't be calculated directly by the FDTD method. Therefore, it is calculated by averaging the values before and after. Then E_z could be summarized as:

$$E_z^n(0,j,k+1/2) = E_z^{n-1}(i,j,k+1/2) + \frac{v\Delta t - \Delta x}{v\Delta t + \Delta x}\left\{E_z^n(1,j,k+1/2) - E_z^{n-1}(0,j,k+1/2)\right\} \quad (2\text{-}77)$$

This is called Mur's first absorbing boundary condition. The above equation applies to electric field components parallel to the absorbing boundary. It has been confirmed that the reflectance is about 0.5% when Mur's first absorbing boundary condition is placed at the tip of the waveguide.

2.2.2.7 Magnetic field distribution

Figures 2-10 and 2-11 show the x-center and z-center cross-sectional views of the static magnetic field strength distribution inside the discharge chamber. This is the magnetic field intensity distribution analyzed using Advanced Science Laboratory, Inc.'s 3D magnetic field analysis software Amaze.

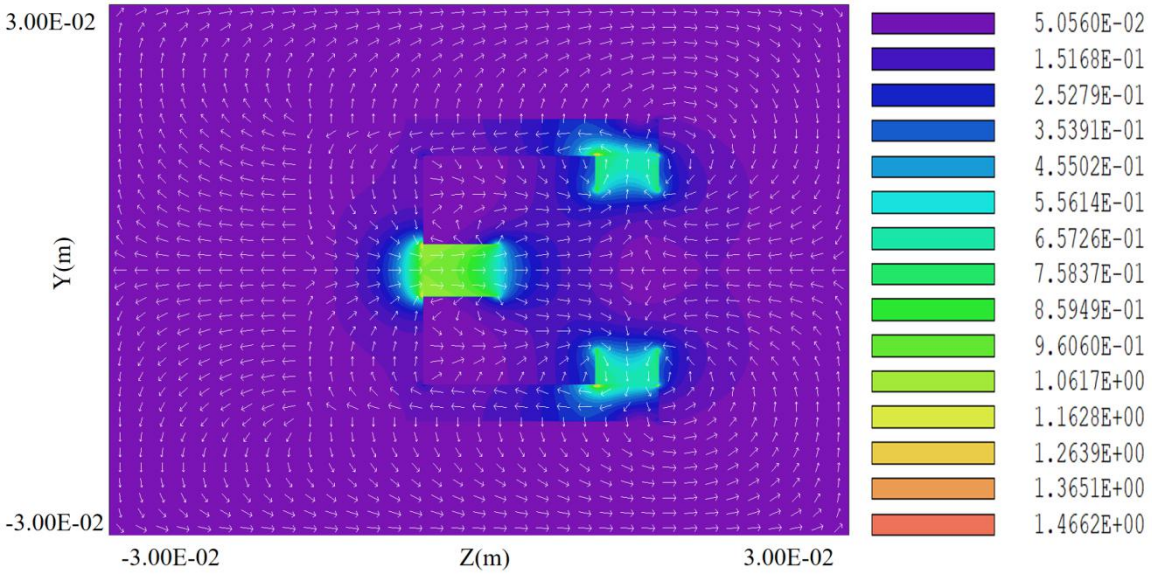

Fig. 2-9 Cross section of magnetic field distribution in discharge chamber(Y-Z plane)

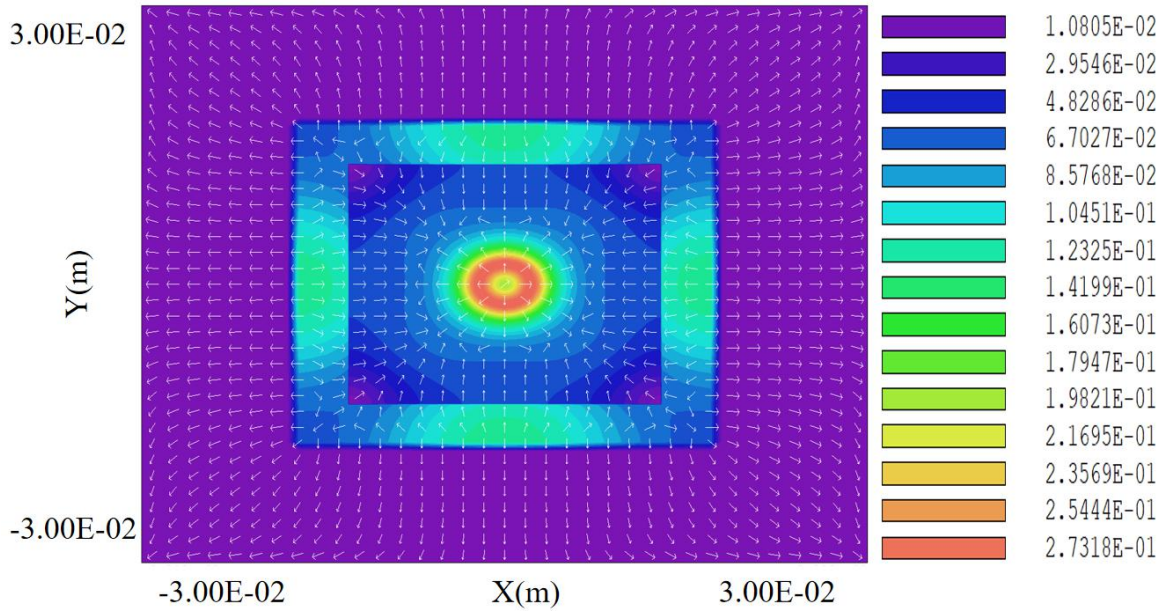

Fig. 2-10 Cross section of magnetic field distribution in discharge chamber(X-Y plane)

2.2.2.8 Physical condition

Table 2-2 shows the physical conditions used in this calculation. The simulation system has similarities with the experimental system developed by our laboratory. So the conditions match the experimental conditions.

The input power was set to 2.0 W. Based on these parameters, the antenna shape was changed and the calculation was performed. The density of neutral particles was determined from the propellant flow rate, the pressure inside the vacuum vessel, and the conductance of the thruster, and was made uniform in the discharge chamber. The initial ion density and electron density were assumed to be equal, and they were evenly distributed in the discharge chamber. The propellant flow rate is considered to be a constant density of neutral particles. This is because a separate DSMC calculation shows that when the propellant mass flow rate is 0.37 mg/s(Xe) / 0.21 mg/s(Ar) , the neutral particle density of the entire propeller is about 8.0×10^{18} m^{-3}/ 4.5×10^{18} m^{-3}, excluding the gas port. The density of neutral particles in the collision calculation has been maintained at this value. The initial ion energy is set to room temperature, and the initial density initial electron energy is set from past experimental data.[2-16)]

Table 2-2 Physical condition

Parameter	Value
Propellant	Xenon/Argon
Mass flow rate	0.37 mg/s / 0.21 mg/s
Microwave frequency	2.45 GHz
Incident power	2.0 W
Neutral particle density	8.4×10^{20} m^{-3}/4.7×10^{20} m^{-3}
Initial electron temperature	2.0 eV

2.2.2.9 Calculation conditions

In the case of simulation dealing with plasma, the mesh size is generally set to the Debye length or less. However, the Debye length inside the thruster is about 20 μm based on calculation of this initial condition. Besides, if the mesh size is set to that extent, the calculation becomes difficult in terms of calculation cost and calculation time. Therefore, in this study, the smallest mesh size that can be calculated is adopted as 0.5 mm, and the number of grids is set to 60 in the x direction, 60 in the y direction, and 50 in the z direction.

Since the electrostatic field is not considered in this study, we do not deal with Debye length shielding and sheath, which are physical phenomena related to Debye length. Therefore, it is considered that the influence of the mesh size larger than the Debye length on the calculation result is small. Details will be described later, but the difference in calculation results when the mesh size was changed is also investigated .

The calculation constraints in FDTD are, based on the mesh size of 0.5 mm, $0.2\,\omega_{pe}^{-1}$= 8.0 × 10^{-12} sec, assuming that the propagation speed of electromagnetic waves is the speed of light, from the Courant condition, 4.8 × 10^{-13} sec or less would be fine, but considering the calculation error, it was set to 1.25 × 10^{-13} sec. The constraints in PIC are 4.0 × 10^{-11} sec as 1/10 of the cyclotron motion period at 100 mT, 7.3 × 10^{-10} sec due to the constraint of collision calculation. When the maximum electron velocity is 100 eV, the Courant condition for not jumping over one cell is 3.45 × 10^{-11} sec, and if it is about 1/10 of that, it is 3.4 × 10^{-12} sec. The strictest constraint among these is the Courant condition, so it is only necessary to satisfy it. Considering only these conditions, the time step of PIC may be about 10 times larger than the time step of FDTD. However, this made the calculation

unstable around the antenna. This is thought to be due to the fact that the large current density around the antenna is used multiple times in his FDTD calculation. Therefore, in this code, FDTD and PIC are calculated in the same time step, and the value is 2.5×10^{-13} sec. Various calculation conditions are shown in Table 2-3.

Table 2-3 Calculation condition

Parameter	Value
Mesh size	0.5 mm
Time step(FDTD)	2.5×10^{-13} s
Weight of super particle	1.0×10^{7}
Number of super particle	1.0×10^{6}
Number of super particle per cell	115
Initial electron temperature	2.0 eV

As for the boundary condition of FDTD, Mur's first absorbing boundary is applied only to the root of the antenna.

Reference

2-1) Sui W, Christensen D A, Durney C H. Extending the two-dimensional FDTD method to hybrid electromagnetic systems with active and passive lumped elements[J]. IEEE Transactions on Microwave Theory and Techniques, 1992, 40(4): 724-730.

2-2) Namiki T. 3-D ADI-FDTD method-unconditionally stable time-domain algorithm for solving full vector Maxwell's equations[J]. IEEE Transactions on Microwave Theory and Techniques, 2000, 48(10): 1743-1748.

2-3) Namiki T. A new FDTD algorithm based on alternating-direction implicit method[J]. IEEE Transactions on Microwave Theory and techniques, 1999, 47(10): 2003-2007.

2-4) Sullivan D M. Electromagnetic simulation using the FDTD method[M]. John Wiley & Sons, 2013.

2-5) Tskhakaya D, Matyash K, Schneider R, et al. The Particle‐In‐Cell Method[J]. Contributions to Plasma Physics, 2007, 47(8‐9): 563-594.

2-6) Arber T D, Bennett K, Brady C S, et al. Contemporary particle-in-cell approach to laser-plasma modelling[J]. Plasma Physics and Controlled Fusion, 2015, 57(11): 113001.

2-7) http://dpc.nifs.ac.jp/aladdin/

2-7) Mathur, D., and C. Badrinathan. "Ionization of xenon by electrons: Partial cross sections for single, double, and triple ionization." Physical Review A 35.3 (1987): 1033.

2-9) Straub, H. C., et al. "Absolute partial and total cross sections for electron-impact ionization of argon from threshold to 1000 eV." Physical Review A 52.2 (1995): 1115.

2-10) Osamu Hashimoto, Takumi Abe: "Introduction to FDTD Time Region Difference Method" (Morikita Publishing, 1996.

2-11) Dey S, Mittra R. A locally conformal finite-difference time-domain (FDTD) algorithm for modeling three-dimensional perfectly conducting objects[J]. IEEE Microwave and Guided Wave Letters, 1997, 7(9): 273-275.

2-12) Toru Uno: “Electromagnetic field and antenna analysis by FDTD method” (Corona Publishing Co., Ltd., 1998.

2-13) Yao L, Wang X, Xu F, et al. Fabrication and impact performance of three-dimensionally integrated microstrip antennas with microstrip and coaxial feeding[J]. Smart Materials and structures, 2009, 18(9): 095034.

2-14) Kumar A, Kaur J, Singh R. Performance analysis of different feeding techniques[J]. International journal of emerging technology and advanced engineering, 2013, 3(3): 884-890.

2-15) Liang F, Wang G, Lin H, et al. Mur absorbing boundary condition for three-step 3-D LOD-FDTD method[J]. IEEE microwave and wireless components letters, 2010, 20(11): 589-591.

2-16) Noriyoshi Onodera, Haruki Takegahara, Kazutaka Nishiyama, et al. Electron emission mechanism of microwave discharge neutralizer [J]. Proceedings of the Japan Society for Aeronautics and Astronautics, 2001, 49 (564): 27-31.

3. Results and discussion

3.1 FDTD-PIC code

The calculation was performed with the FDTD-PIC code with the electrons arranged. Each figure shows a zy cross section of x = 14 mm and a xy cross section of z = 19.0 mm.

3.2 Electric field strength distribution

Figure 3-1 to Figure 3-4 show the snapshot of the electric field intensity distribution at 75.0 ns. A strong electric field of about 7.0×10^4 V/m is generated around the antenna in both two cases.

In the magnetic mirror area between the center magnets and the permanent magnets, there's an high intensity electric field gathing as a conical configuration . It can be seen that since the input voltage is both 12.0 V, there is no significant difference in the electric field intensity distribution based on the two different propellants, and the case of argon may slightly win the intensity maximum. This may be because the antenna uses the most basic linear antenna. If other antennas such as cross, disk, star, and L are considered for re-simulation, it is possible to find differences in the distribution range of the strong electric field.

At the same time, the reason for the appearance of the cone electric field is not clear. This is the first time a similar phenomenon has been found in numerical simulations. The possible reason is that the distance between the central magnet and the permanent magnet is close, so the magnetic field affects the electric field distribution in the magnetic mirror area.

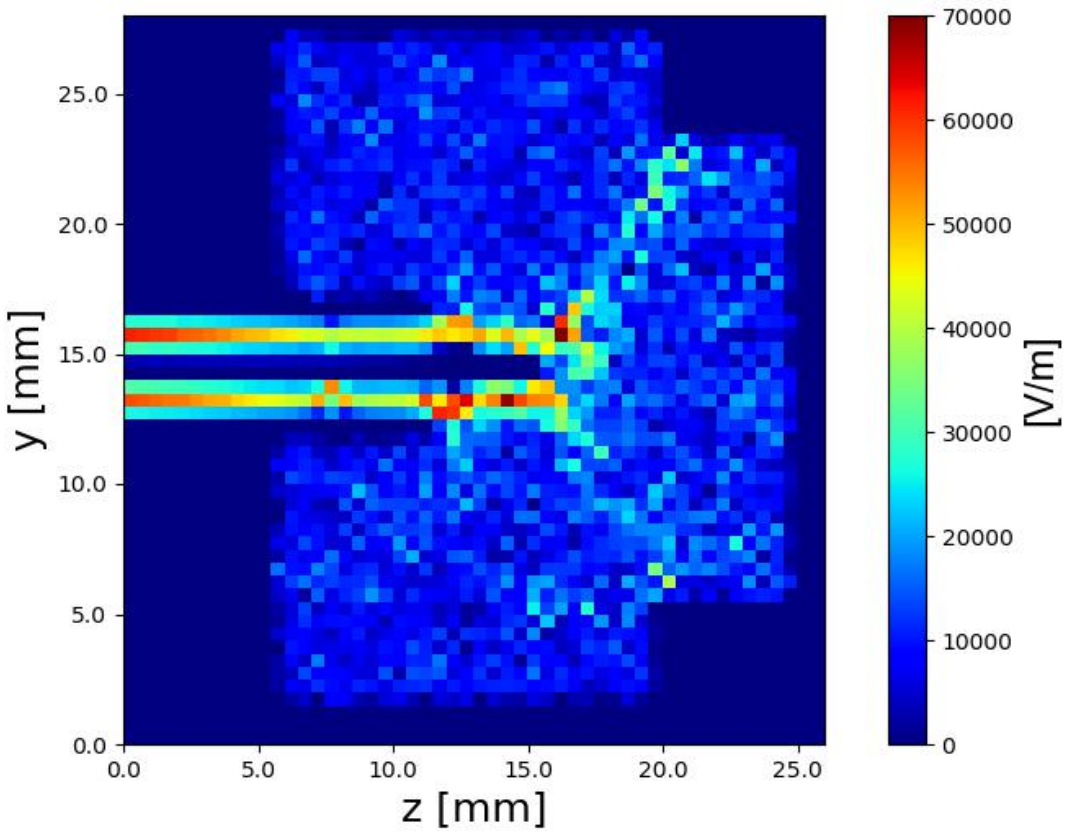

Fig. 3-1 Electric field strength distribution of Xenon(Y-Z plane)

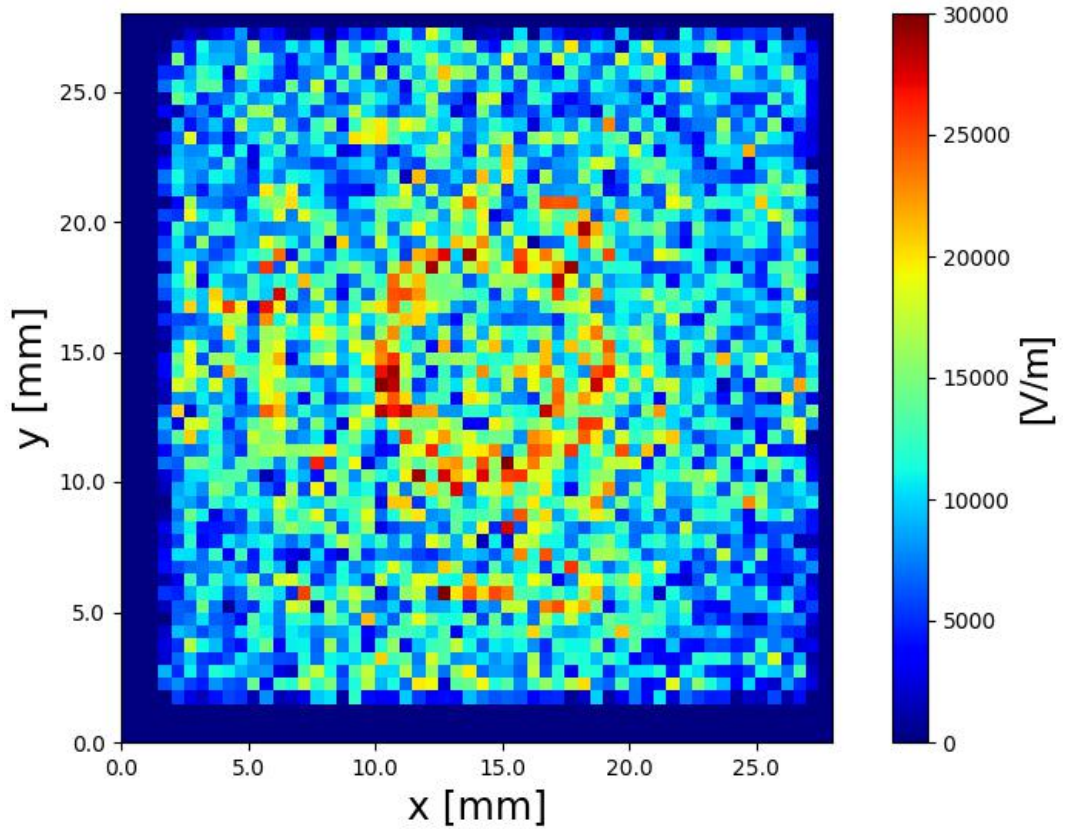

Fig. 3-2 Electric field strength distribution of Xenon(X-Y plane)

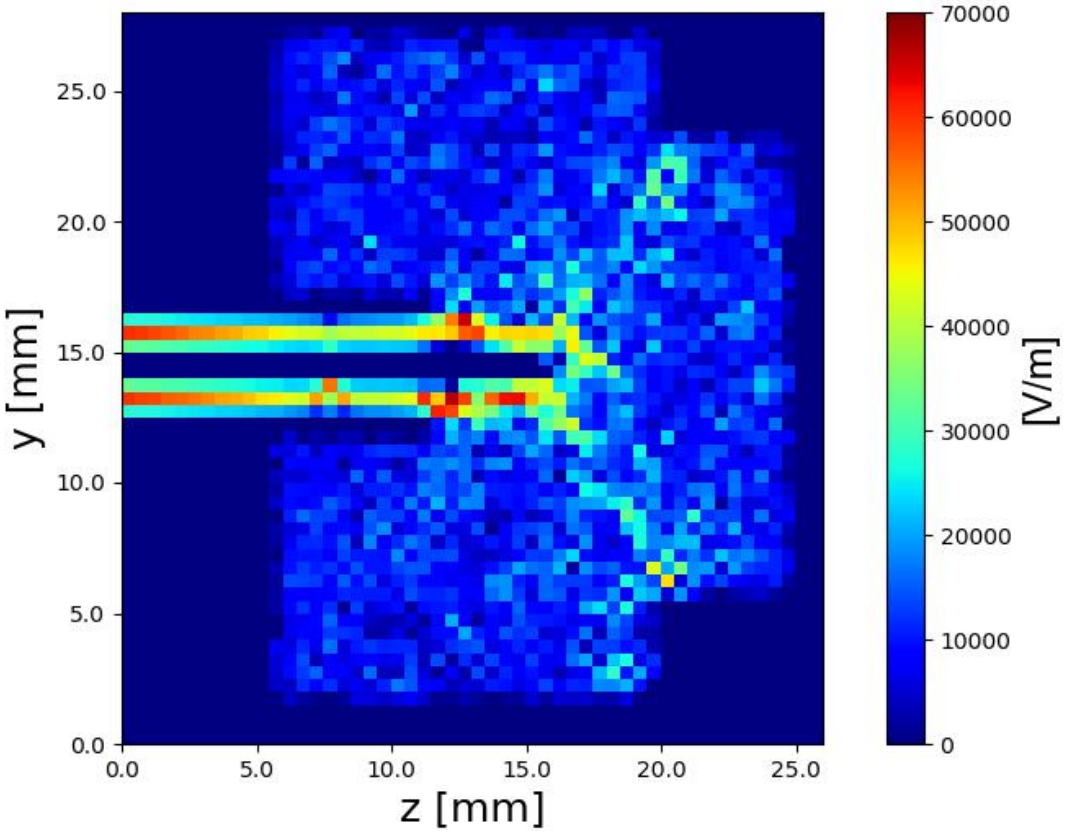

Fig. 3-3 Electric field strength distribution of Argon(Y-Z plane)

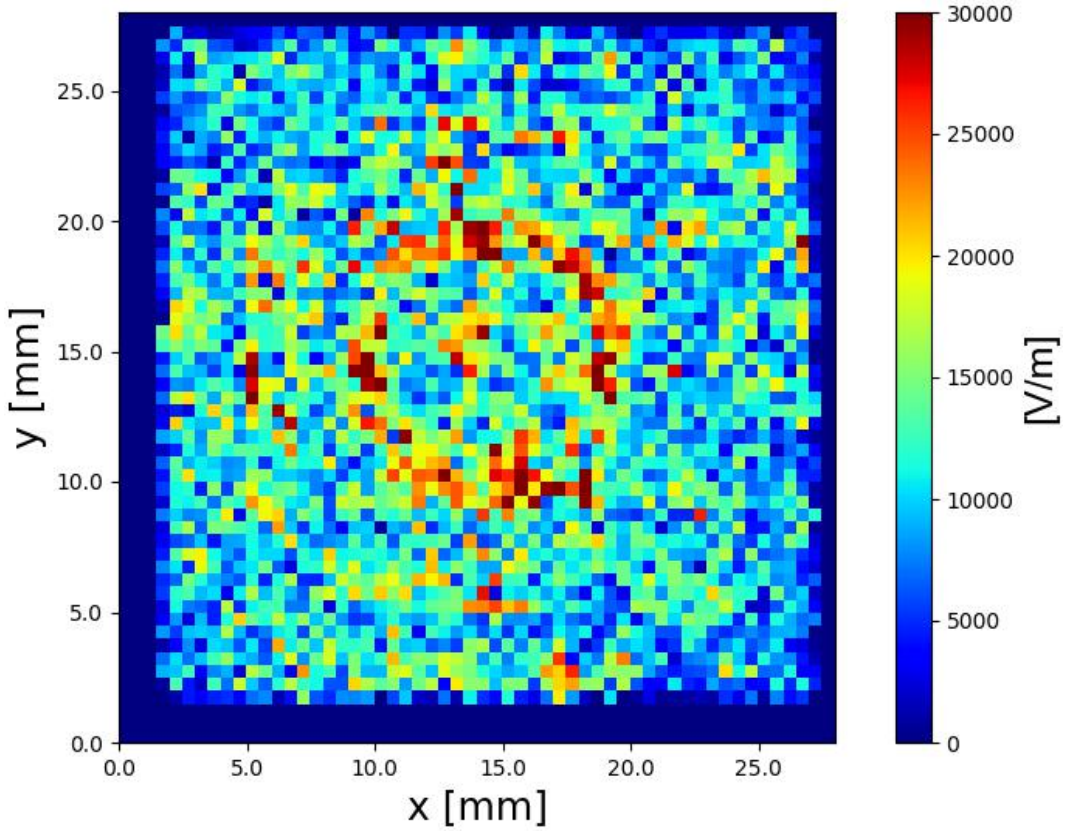

Fig. 3-4 Electric field strength distribution of Argon(X-Y plane)

3.3 Electron number density distribution

Figure 3-5 through Figure 3-8 show the snapshot of electron density distribution at 75.0 ns for each propellant. Typically, the electron density near the antenna and walls is low. But the distribution of both cases look pretty uniformly. Also, again, there is no discernible difference in the electron density distributions based on the two different propellants. These two phenomenons may be due to the short analysis time, not enough ionization to be observed, the plasma inside the chamber also did not reach steady state, so later analysis times need to be extended to see differences in electron density.

Generally speaking, it is necessary to extend the computation time to hundreds of microseconds in order to make the plasma reach a preliminary steady state and obtain a relatively accurate particle distribution.

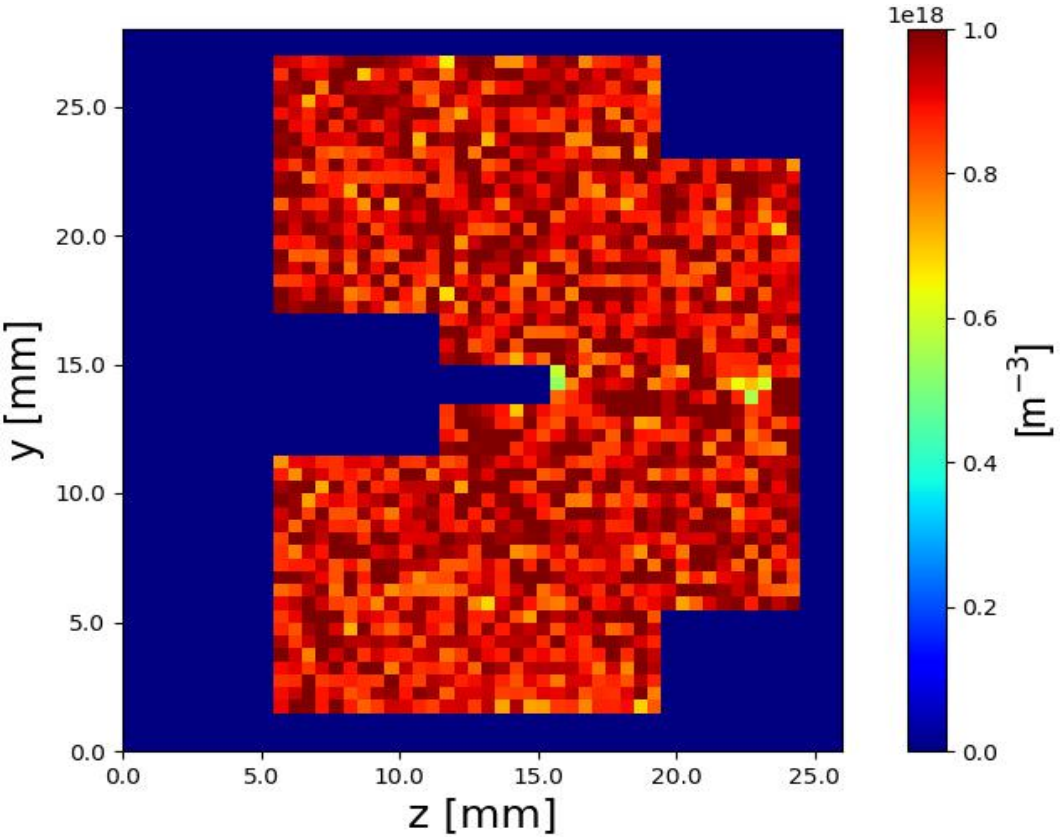

Fig. 3-5: Density distribution of Xenon(Y-Z plane)

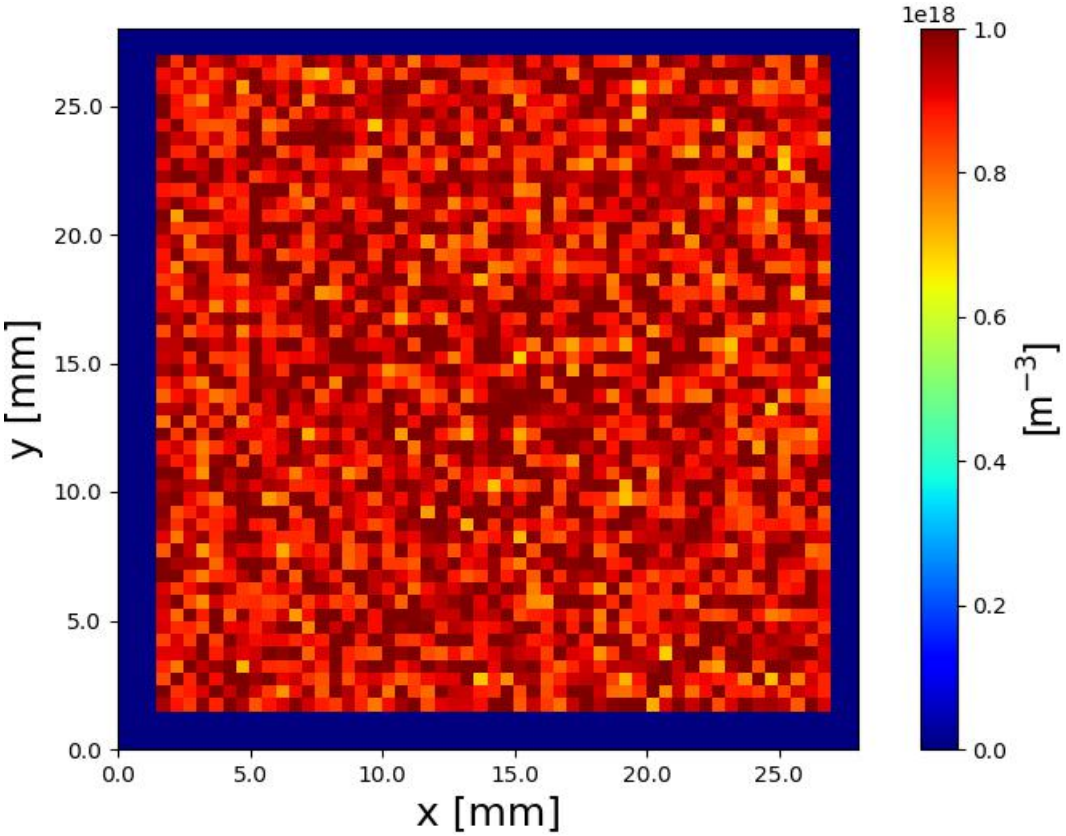

Fig. 3-6: Density distribution of Xenon(x-y plane).

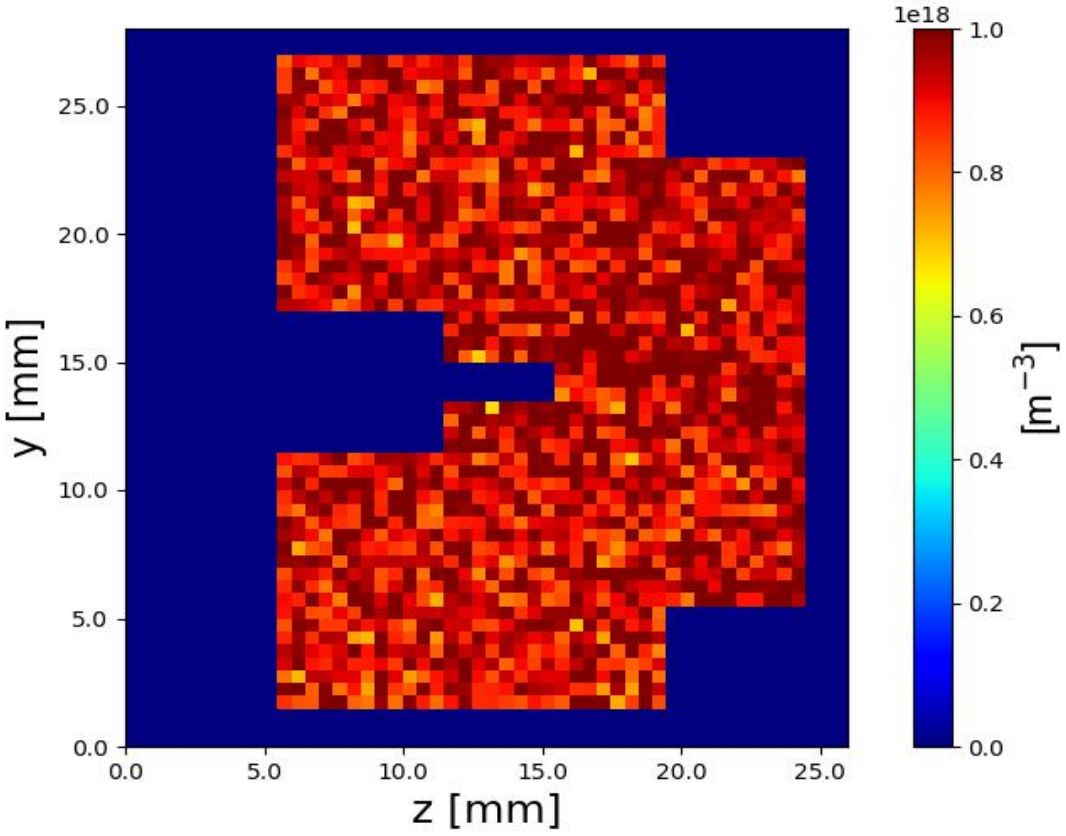

Fig. 3-7: Density distribution of Argon(Y-Z plane)

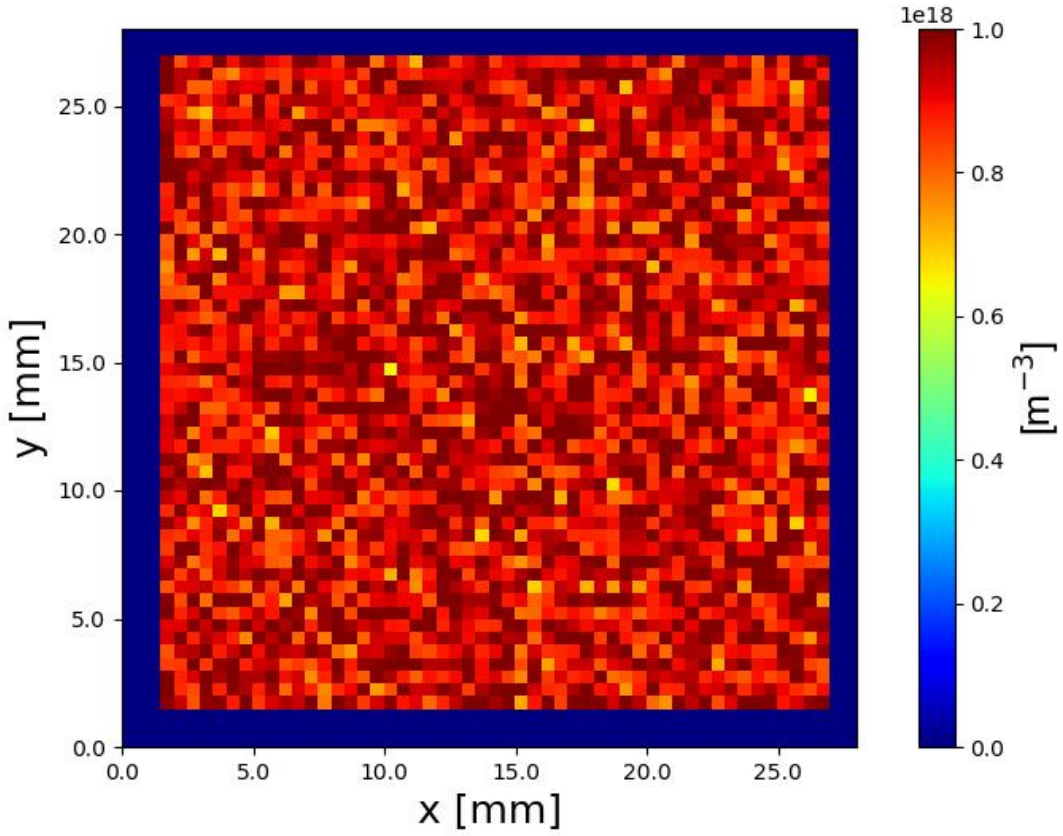

Fig. 3-8: Density distribution of Argon(X-Y plane)

3.4 Electron averaged energy distribution

Under the same input voltage (12.0 V), in the case of argon, the average energy of electrons is much higher than that in the case of xenon in terms of both the energy extreme and the diffusion range. Although this is strong evidence that argon allows the electrons in the discharge chamber to accept more energy from the microwaves, and thus matches the expected estimates of this simulation, the difference seems to be too large. At the same time, the distribution of the average electron energy does not correspond to the conical distribution of the electric field in Section 3.2, but tends to fill the region relatively close to the right boundary of the chamber.

One possible conjecture is that the neutral particle densities used in this simulation came from previous experiments. Therefore, after setting different impedances and mass flow rates, through DSMC calculations, different particle densities are used for xenon and argon. This could lead to differences in the plasma potential, which changes the reflectivity of the plasma when it receives microwave energy. However, the data currently available is not

enough to prove that the speculation is correct. Therefore, in the subsequent numerical simulation stage, it is necessary to comprehensively consider various factors to find the reason for the difference in energy distribution.

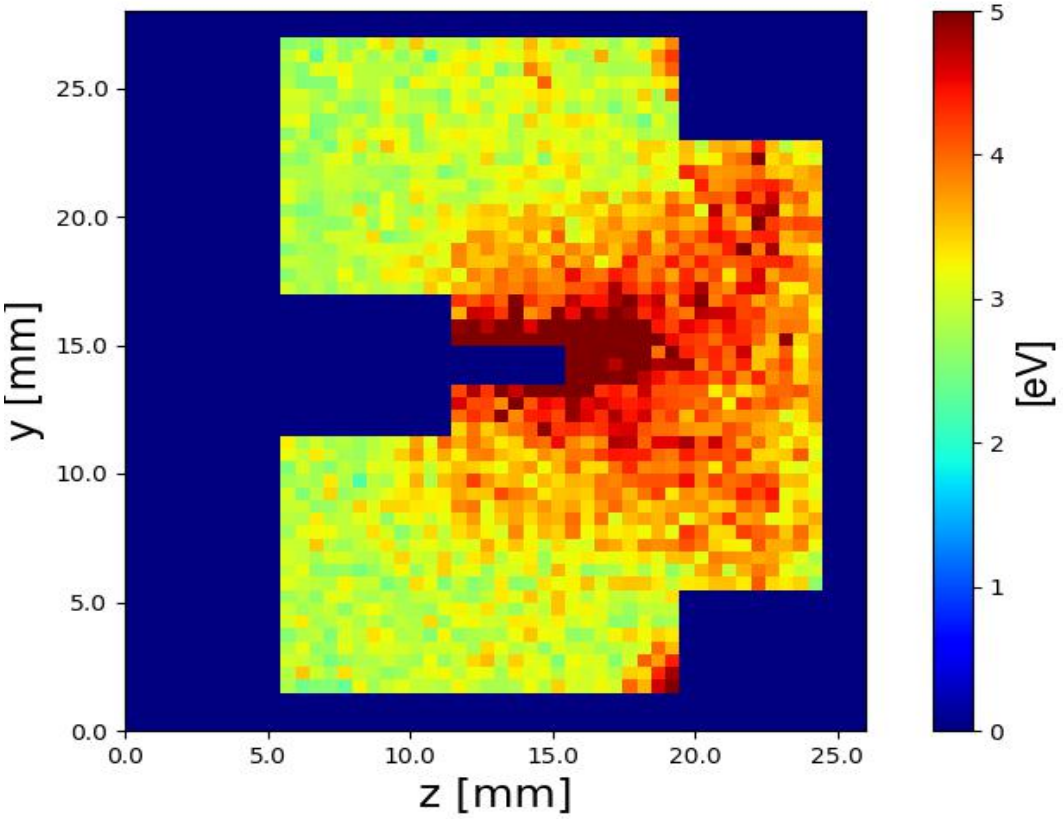

Fig. 3-9: Averaged energy distribution of Xenon(Y-Z plane)

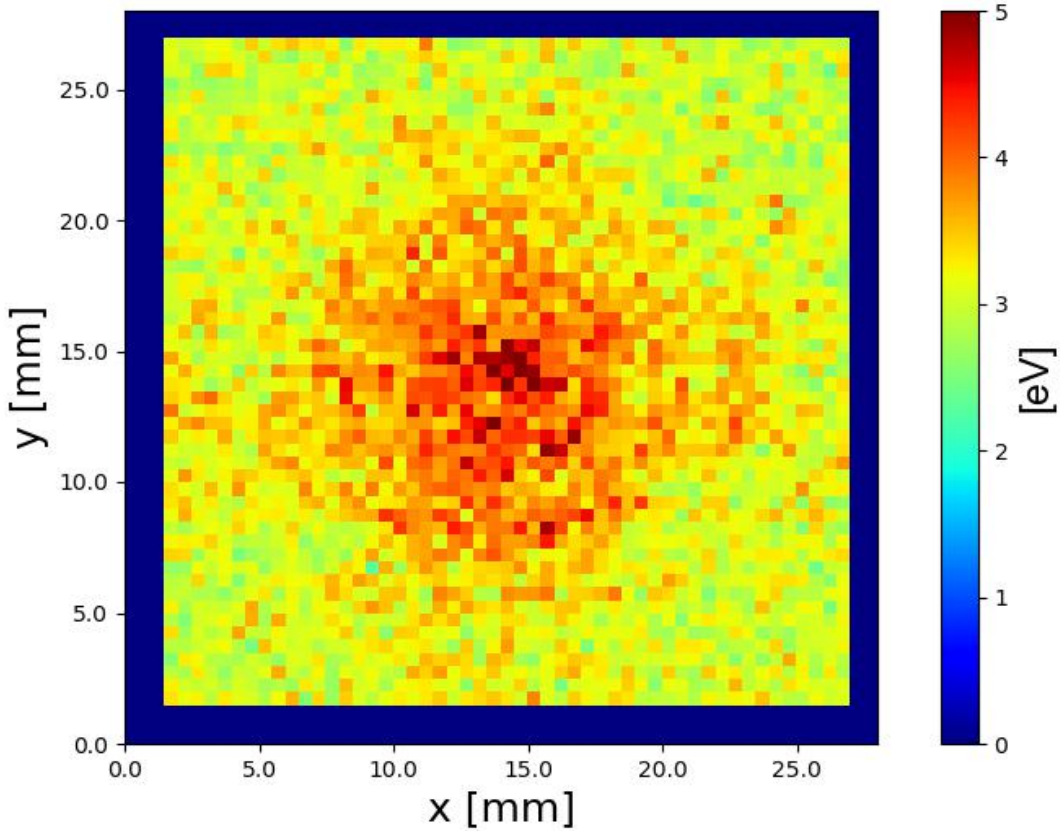

Fig. 3-10: Averaged energy distribution of Xenon(X-Y plane)

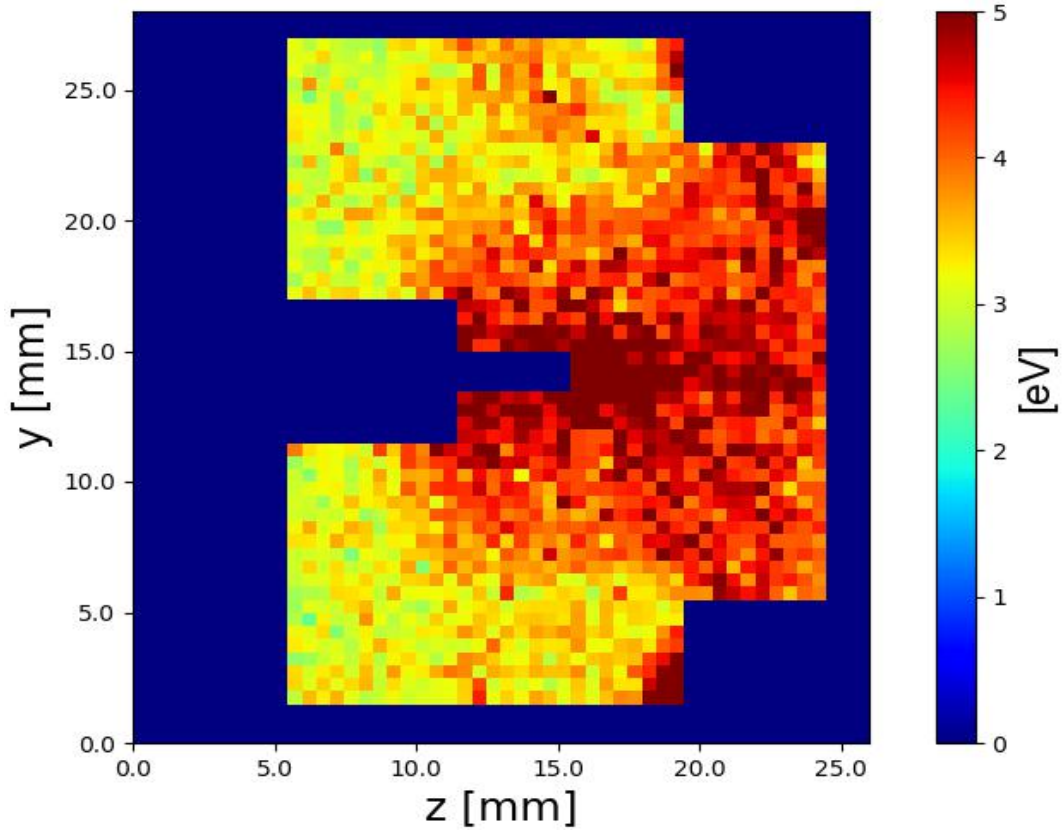

Fig. 3-11: Averaged energy distribution of Argon(Y-Z plane)

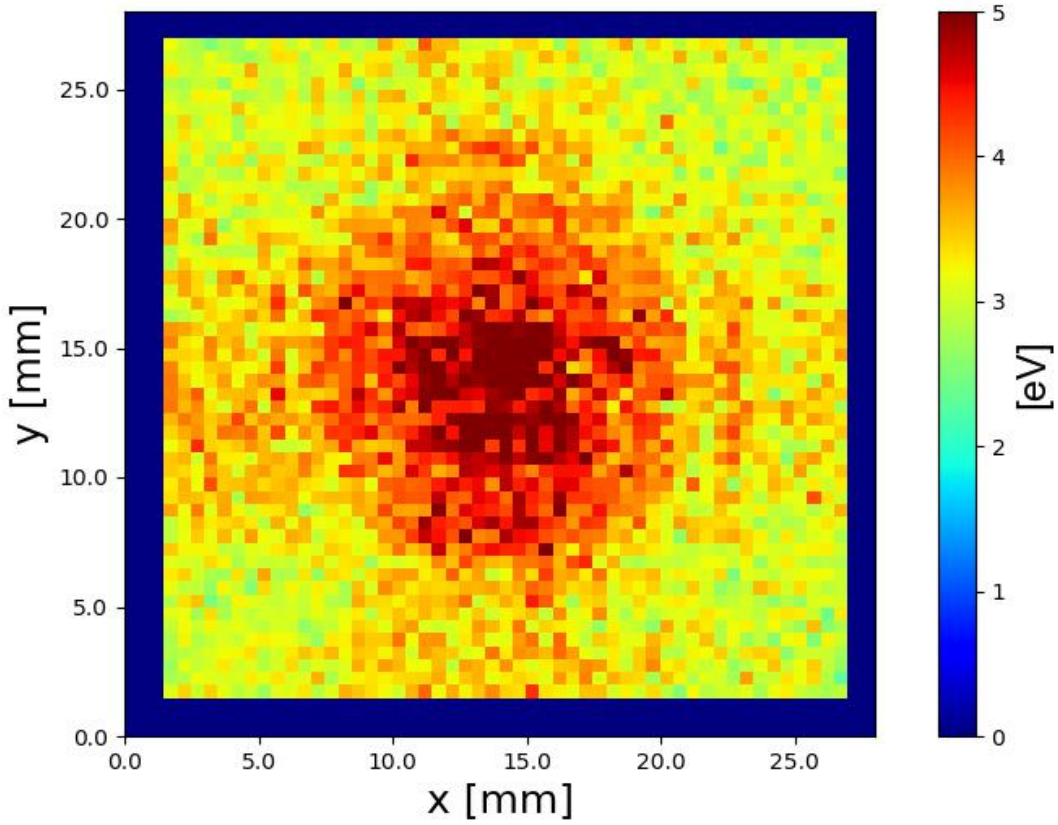

Fig. 3-12: Averaged energy distribution of Argon(X-Y plane)

3.5 Net power

In order to find out the reasons for the huge difference in the electron energy distribution in the case of xenon and argon in Section 3.4, this study compared the microwave incident power, reflectivity and net power under different input voltages from 4.5 V to 12.0 V, and obtained Table. 3-1 with Fig. 3-13.

Among them, S1 represents the net power measured on the plane on the right side of the feed point, and S2 represents the net power measured on the plane on the left side of the feed point. The microwave incident power represents the power transmitted by the microwave to the plasma through the antenna, and the reflected power represents the reflected power caused by impedance during the propagation process. (Please refer to chapter 2.2.2.4 Measurement of input energy for details)

Table.3-1

	Net Power S1[W]		Net Power S2[W]		Incident Power[W]		Reflected Power[W]		Reflection Ratio(%)	
Input voltage	Xe	Ar	Xe	Ar	Xe	Ar	Xe	Ar	Xe	Ar
4.50	1.7	3.2	-7.9	-8.0	4.8	5.6	-3.1	-2.4	64.8	42.3
6.25	3.2	6.4	-15.1	-15.2	9.2	10.8	-6.0	-4.4	64.7	40.8
7.00	4.0	7.9	-19.1	-19.3	11.5	13.6	-7.5	-5.7	65.2	41.7
8.00	5.3	10.4	-25.0	-25.0	15.1	17.7	-9.9	-7.3	65.1	41.4
9.00	6.8	13.1	-31.5	-31.7	19.2	22.4	-12.4	-9.3	64.4	41.4
10.0	8.2	16.3	-39.3	-39.1	23.7	27.7	-15.5	-11.4	65.5	41.1
12.0	12.2	23.4	-56.1	-56.1	34.1	39.8	-21.9	-16.4	64.2	41.2

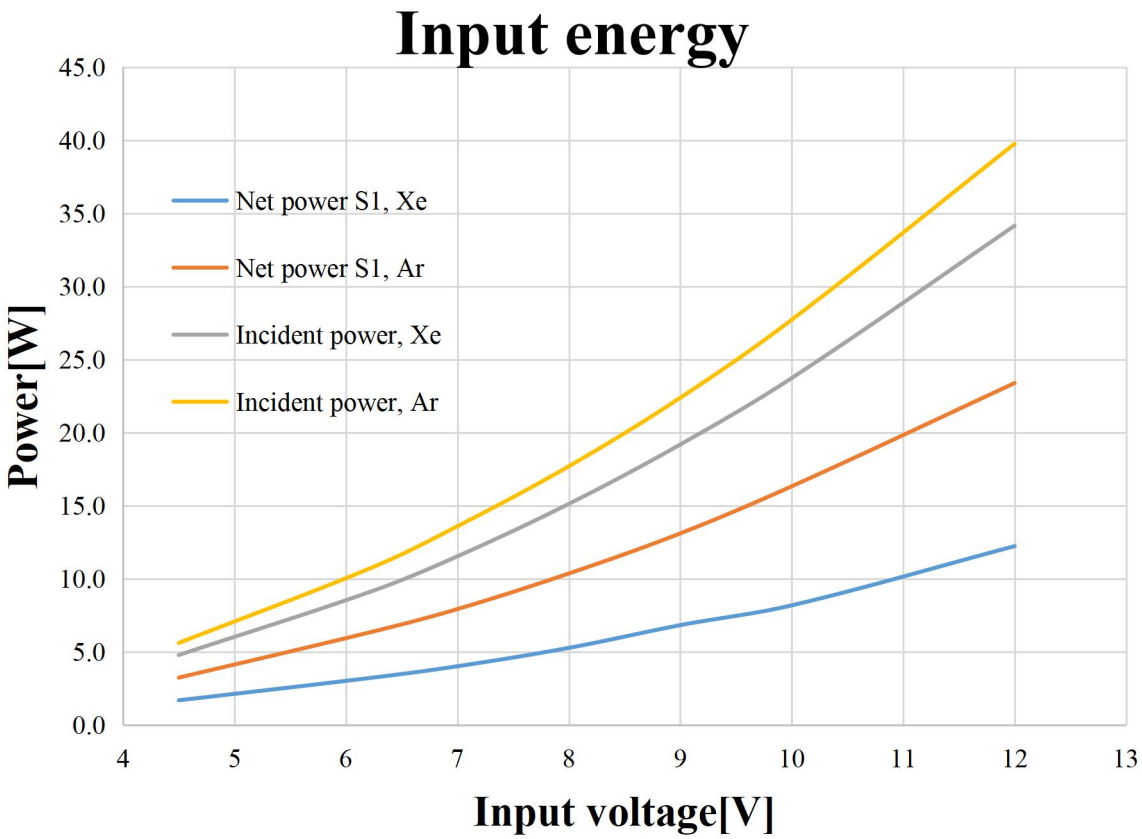

Fig. 3-13 Input energy comparison

It can be seen that even under the same input voltage, the Net power and the microwave incident power are not consistent under the conditions of argon and xenon. Moreover, the power in the argon case is better than that of the xenon. This should be due to the different

reflectivity. From Table. 3-1, it can be seen that no matter what the input voltage is, the reflectivity of the argon case remains around 41%, while the reflectivity of the xenon case remains around 65%. Then, due to the difference in reflectivity, no matter what the input voltage is, the incident microwave power in the xenon case is smaller than that in the argon case. This explains why the argon case has such a huge advantage in the distribution of the average electron energy in Section 3.4.

4. Conclusion

On the basis of many previous studies, a new way to improve the ion engine is proposed: numerical simulation is used to simulate the plasma behavior inside the discharge chamber of the ion engine, so as to obtain the performance of different propellants and compare them.

The prior simulation research on the ion engine in this laboratory and other laboratories mainly focuses on the internal configuration of the discharge chamber, such as changing the shape and size of the discharge chamber, or adjusting the interior of the discharge chamber by increasing or decreasing the number of permanent magnets and changing the position. the magnetic field strength. However, few studies have focused on simulating the plasma behavior inside the discharge chamber with different propellants.
Based on the previous research, this study preliminarily compared the performance of xenon and argon in the new cubic discharge chamber model, and gave a reasonable explanation for the observed physical phenomena.

In the method of numerical analysis, the code of FDTD and PIC coupling is used, and the different parameters of xenon and argon are set by adjusting different collision cross-sections, and the electric field intensity distribution and electron density distribution inside the discharge chamber at 75.0 ns are obtained. , and the average electron energy distribution. And by comparing the performance differences between xenon and argon cases, the possibility of argon being used as xenon to replace ion engine propellant is given. It also gives directions for the next step to quantitatively analyze the performance differences between argon and xenon and to improve the design of the ion engine discharge chamber in the future.

5. Acknowledgement

First of all, I would like to express my deepest thanks to Professor Yamamoto Naoji for giving me an opportunity to enter the field of space propulsion, and for important guidance in the thesis writing, numerical simulation, scientific research reading and many other aspects over the past two years. I'm also very grateful to Assistant Professor Morita Taichi for his polite and rigorous questions at the group meeting, as well as careful reminders and suggestions in daily discussions. In addition, their rigorous academic attitude and scientific research spirit are also a role model for me forever, which will benefit me a lot in my future study and work. I'm deeply grateful to Ouchida Eiko , the administrative assistant who supported our laboratory through administrative procedures and made our laboratory a bright atmosphere. I would like to express my deep gratitude to Professor Hiroshi Idei and Associate Professor Yusuke Kosuga of the Interdisciplinary Graduate School of Engineering Sciences, Kyushu University, who were in charge of the deputy review of this paper and gave me very polite comments on my poor paper. I would like to express my most sincere thanks to Mr. Hiroike Naruya. Mr. Hiroike is not only one of the important guides for me to enter the field of numerical simulation, but without his help in the field of numerical simulation and electromagnetic field, this graduation thesis would not be possible. I would also like to thank Mr. Kojima Tomihiko for his many help in day-to-day research and mastering supercomputer systems, and for clearing up a lot of confusion for me.

Many thanks to Mr. Kojima Takuto, Mr. Matsuo Suzuto, Mr. Kawabe Tomo, Mr. Ikebe Masaki, Mr. Kuramoto Eisuke, who taught me a lot in daily conversation, which helped me greatly improve my Japanese and overcome the communication barriers in my heart. I would like to thank all the M1 and B4 students who spent a fulfilling time together in the laboratory.

Last but not least, I would like to sincerely thank my family and friends who are my strong backing. They have always encouraged and supported me to overcome the difficulties within these years.